

1 **Petrogenesis of the Triassic granitoids from the East Kunlun Orogenic**
2 **Belt, NW China: Implications for continental crust growth from syn-**
3 **collisional to post-collisional setting**

4
5 Juanjuan Kong ^{a, b*}, Yaoling Niu ^{b, c, d*}, Yan Hu ^e, Yu Zhang ^b, Fengli Shao ^f

6 ^a College of Ocean Science and Engineering, Shandong University of Science and
7 Technology, Qingdao 266590, China

8 ^b Laboratory for Marine Geology, Qingdao National Laboratory for Marine Science and
9 Technology, Qingdao 266061, China

10 ^c Department of Earth Sciences, Durham University, Durham DH1 3LE, UK

11 ^d State Key Laboratory of Geological Processes and Mineral Resources, and School of
12 Earth Science and Mineral Resources, China University of Geosciences, Beijing
13 100083, China

14 ^e Geology Survey Institute of Gansu Province, Lanzhou 730000, China

15 ^f Linyi University, Linyi 276000, China

16

17 *Corresponding authors:

18 Miss Juanjuan Kong (juanjuan0317@foxmail.com)

19 Professor Yaoling Niu (yaoling.niu@durham.ac.uk)

20

21 **Abstract**

22 The Triassic granitoids are widespread in the eastern section of the East Kunlun
23 Orogenic Belt (EKOB) on the northern Tibetan Plateau. These granitoids well record
24 the evolution of the Paleo-Tethys oceans (named as A'nyemaqen Ocean in the EKOB).
25 Our new zircon U-Pb data together with ages in literature show that these granitoids
26 represent long-lasting magmatism from the early (T_1 , ~ 251-248 Ma), middle (T_2 , ~
27 247-238 Ma) to late (T_3 , ~ 234-214 Ma) Triassic. The Triassic granitoids display calc-
28 alkaline I-type granite affinities and hybrid mantle-crust geochemical signatures. The
29 T_1 granitoids possess andesitic to felsic bulk continental crust (BCC)-like chemical
30 composition (e.g., enriched in Rb, K and Pb, depleted in Nb, Ta, Sr, P and Ti), coupled
31 with high I_{Sr} (0.7067-0.7148), negative $\epsilon_{Nd(t)}$ (-7.32 to -1.66) and negative to positive
32 $\epsilon_{Hf(t)}$ (-5.11 to 3.59) as well as $(Dy/Yb)_N = 1.1$, suggesting that the T_1 granitoids were
33 formed by melting of the subducted A'nyemaqen oceanic crust with terrigenous
34 sediments under the amphibolite facies conditions in a syn-collisional setting. The T_2
35 and T_3 granitoids may be originated from a relatively homogeneous source with almost
36 consistent mean values of I_{Sr} (0.7136 [T_2], 0.7094 [T_3]), $\epsilon_{Nd(t)}$ (-5.83 [T_2], -5.97 [T_3])
37 and $\epsilon_{Hf(t)}$ (-3.52 [T_2], -3.58 [T_3]). They present garnet signature of adakitic rocks and
38 can be explained by partial melting of the juvenile mafic lower continental crust and
39 mixing with upper crustal components during magma ascent. This process is considered
40 to be associated with post-collisional extension which induced by asthenosphere
41 upwelling and mantle melting, providing heat for mafic lower crust melting to form T_2

42 and T₃ granitoids. The T₁ granitoids with mantle signatures (e.g. $\epsilon_{\text{Hf(t)}}$ > 0) as well as
43 BCC-like compositions represent a net flux of juvenile dioritic to granitic materials
44 adding to the continental crust, in support of the hypothesis of “continental collision
45 zones are primary sites for net continental crust growth” along the EKOB. The genetic
46 link between T₂ and T₃ granitoids means the EKOB had transformed to post-collisional
47 setting since the middle Triassic (~ 247 Ma). All these hypotheses are conceptually
48 important for understanding the origin of the juvenile crust and continental crustal
49 growth through magmatism from syn-collisional to post-collisional settings.

50

51

52 **Keywords:** East Kunlun Orogenic Belt; syn-collisional granitoids; post-collisional
53 granitoids; continental crust growth; A’nyemaqen Ocean

54

55 1. Introduction

56 Granitoid batholiths are the most abundant constituent of continental crust, and
57 their origin is essential for understanding the evolution and differentiation of the
58 continental crust (Luo *et al.*, 2015). The East Kunlun Orogenic Belt (EKOB) as one of
59 the major magmatic belts on the Tibetan Plateau is considered to undergo multi-cycle
60 tectonic evolution and record the evolution of the Proto- and Paleo-Tethys oceans from
61 the Early Paleozoic to the Early Mesozoic (Mo *et al.*, 2007; Xiong *et al.*, 2014).
62 Widespread granitoid batholiths of two episodes, i.e. Early Paleozoic and Late

63 Paleozoic-Triassic in the EKOB formed in volcanic-arc, syn-collisional and post-
64 collisional settings have supplied much information to help understand the geological
65 evolution of the Proto- and Paleo-Tethys oceans over the past three decades (Jiang *et*
66 *al.*, 1992; Huang *et al.*, 2014; Shao *et al.*, 2017). We focus on the Triassic granitoids in
67 the eastern section of the EKOB where previous studies have revealed the history of
68 Paleo-Tethys orogenic events of 270-195 Ma (Chen *et al.*, 2007; Sun *et al.*, 2009; Xiong
69 *et al.*, 2012; Zhang *et al.*, 2012; Xu *et al.*, 2015; Ren *et al.*, 2016). Despite the large
70 number of recent studies on the tectonic evolution of the Paleo-Tethys, many
71 uncertainties and controversies remain (Mo *et al.*, 2007; Pan *et al.*, 2012; Xia *et al.*,
72 2015). Moreover, these studies concentrated on scattered/individual intrusions, lacking
73 systemic chronology, geochemistry, and especially isotopic investigations.

74 Continental crustal growth is widely considered to be associated with the
75 subduction-zone magmatism because of the arc-like incompatible element signature of
76 the bulk continental crust (BCC) (e.g., enrichment in U, K and Pb, depletion in Nb, Ta
77 and Ti; Niu *et al.*, 2013), which is termed “island arc model” (Taylor, 1967). However,
78 the standard “island arc model” has many difficulties (Niu & O’Hara, 2009; Niu *et al.*,
79 2013), aiming at which Niu and co-workers proposed a testable hypothesis “continental
80 collision zones are primary sites of net continental crustal growth”. Because of this and
81 on the basis of their detailed studies of the Linzizong syncollisional volcanic sequence
82 in southern Tibet (Mo *et al.*, 2008), this hypothesis has been tested with success in
83 several orogenic belts (Mo *et al.*, 2008; Niu & O’Hara, 2009; Niu *et al.*, 2013; Huang

84 *et al.*, 2014; Zhang *et al.*, 2016; Kong *et al.*, 2017; Shao *et al.*, 2017), including the
85 preliminary study of the EKOB syn-collisional granitoids. Furthermore, comparison
86 between the syn- and post-collisional granitoids in the Triassic offers important
87 information for the continental crust growth in different context of the orogenesis.

88 In this paper, we systemically present new geochemical and geochronological data
89 for the granitoids in the eastern section of the EKOB. Our new data, together with age
90 data from the literature, shed light on the petrogenesis of the granitoids from the syn-
91 to post-collisional settings and provide constraints on the evolution of the Paleo-Tethys
92 oceans and continental crustal growth in the EKOB.

93

94 **2. Geological setting and samples**

95 The EKOB is located south of the Kunlun-Qaidam terrane constrained between
96 the south Qilian suture (SQS) to the north and the A'nyemaqen-Kunlun-Mutztagh
97 suture (AKMS) in the south on the northern Tibet Plateau. The globally unique Tibetan
98 Plateau has been amalgamated through multiple continental collision events, resulting
99 in progressively younger sutures from northeast (Early Paleozoic) to southwest
100 (Cenozoic) (Fig. 1a; Niu *et al.*, 2013). The northern Tibet Plateau is thus the ideal site
101 for studying the processes of continental collision and geological consequences. The
102 EKOB is bounded by the Qaidam Basin to the north and Baryan Har-Songpan Ganze
103 terrane (BH-SG) to the south, extending W-E for ~ 1500 km (Fig. 1b; Jiang *et al.*, 1992;
104 Ding *et al.*, 2014). Three sub-units (the northern, middle and southern zone) have been

105 recognized in the EKOB, separated by two subparallel faults (Central and South Kunlun
106 Fault) offset by the Altun Tagh sinistral strike-slip fault in the west (Fig. 1b; Jiang *et al.*,
107 1992; Liu *et al.*, 2004). Our study area is in the eastern section of the EKOB with middle
108 and southern magmatic zones well exposed. The middle zone is dominated by Late
109 Paleozoic and Triassic granitoids. It also contains Precambrian metamorphic basement,
110 Devonian sandstones, conglomerates and Carboniferous marine limestones and clastic
111 sedimentary rocks. Comparatively, the southern zone is a more complex fold belt,
112 which is divided into western Late Paleozoic fold group, middle Precambrian uplift and
113 eastern Paleozoic and Triassic fold group. The basement is dominated by the
114 Mesoarchean-Mesoproterozoic Jinshuikou Group in the middle zone and the
115 Paleoproterozoic Kuhai Group in the southern zone (Fig. 1c). The Jinshuikou Group,
116 which comprises the lower Mesoarchean-Paleoproterozoic Baishahe Formation and the
117 upper Mesoproterozoic Xiaomiao Formation (Wang *et al.*, 2004; Chen *et al.*, 2011).
118 The Jinshuikou Group is consist of gneisses, marbles, greenschists, amphibolites,
119 migmatites and quartzites and had been involved into later granulite-facies
120 metamorphism and anatexis during 460-402Ma (Zhang *et al.*, 2003; Wang *et al.*, 2007).
121 The Kuhai Group is a metamorphic rock series of amphibolite facies forming during
122 2330-1441 Ma, which consist of gneiss, plagioclase amphibolite, quartz schist and
123 migmatites (Wang *et al.*, 2007). Two ophiolite belts distributed along the Central and
124 South Kunlun Fault, the Nuomuhong-Qingshuiquan ophiolite belt (NQO) extending
125 along the south of the Central Kunlun Fault and the A'nyemaqen ophiolite belt (AMO)

126 in the southern margin of the EKOB (Bian *et al.*, 2001; Jiang *et al.*, 1992; Zhang *et al.*,
127 2012). It is accepted that the NQO formed in the Early Paleozoic, indicating the closure
128 of Central Kunlun Ocean (Yang *et al.*, 1996; Li *et al.*, 2012). While the formation age
129 of the AMO is relatively complex. Many studies have confirmed that the AMO
130 represent two stages of ocean closing, i.e. Early Paleozoic (~467Ma) Qinling-Qilian-
131 Kunlun Ocean (Bian *et al.*, 2004); Late Paleozoic to Middle Triassic (~308-260Ma)
132 Paleo-Tethys Ocean (Jiang *et al.*, 1992; Yang *et al.*, 2009).

133 The EKOB preserves geological records of the Early Paleozoic Caledonian cycles
134 and the Late Paleozoic to Early Mesozoic Variscan-Indosinian cycle. The Early
135 Paleozoic (500-400 Ma) granitoids are comparable with those in the North Qilian
136 orogenic belt (Mo *et al.*, 2007). The Permian-Triassic granitoids are dominant in the
137 EKOB (~25,000 km²) and account for 50% of the total outcrop area of the granitoids
138 (Fig. 1c, Jiang *et al.*, 1992; Zhang *et al.*, 2014).

139 Samples of this study are collected from the eastern section of the EKOB, which
140 extend W-E for ~ 300 km and distribute in the Middle and Southern Zones (Fig. 1c).
141 They are intermediate- to coarse- grained granites to granodiorites (Fig.2) with mineral
142 assemblage of quartz + potash feldspar + plagioclase + amphibole + biotite + magnetite
143 and accessory minerals of apatite and zircon (see Table 1 for detail). Fine-grained
144 dioritic mafic magmatic enclaves (MMEs) are dispersed in the pluton (Fig.2a, b).

145
146 **3. Analytical methods**

147 *3.1. Zircon U-Pb dating*

148 Zircons from seven samples were separated for U-Pb dating using combined
149 methods of heavy liquid and magnetic techniques. The zircon internal structure was
150 examined using cathodoluminescence (CL) imaging on a FEI Quanta 450 FEG
151 scanning electron microscope (SEM) at the State Key Laboratory of Geological
152 Processes and Mineral Resources (GPMR), China University of Geosciences, Wuhan.
153 U-Pb dating was conducted by laser ablation inductively coupled plasma mass
154 spectrometry (LA-ICP-MS) at the same laboratory, using a 32 µm spot size. Zircon
155 91500 was used as the external standard (Wiedenbeck *et al.*, 1995). Each block of 6
156 unknowns was bracketed by analyses of the standards. Off-line selection and integration
157 of background and analyte signals, and time-drift correction and quantitative calibration
158 for trace element analyses and U-Pb dating were performed by ICP-MS-Data-Cal (Liu
159 *et al.*, 2010). Eighteen points of each sample were chosen for LA-ICP-MS U-Pb
160 analysis and their results are given in Appendix A. Concordia diagrams and weighted
161 mean calculations were processed using the Isoplot/Ex_version 4.15 program (Ludwig,
162 2012). Concordia diagrams and representative CL images of seven samples are shown
163 in Figure 3.

164

165 *3.2. Major and trace elements*

166 Twenty-five freshest samples were chosen for elemental analysis. Weathered
167 surfaces and pen saw marks were removed, cleaned, and ultrasonically cleaned with

168 Milli-Q water and dried before powdered using an agate mill into ~200-mesh in a clean
169 environment.

170 Major elements were determined using a Leeman Prodigy inductively coupled
171 plasma-optical emission spectroscopy (ICP-OES) system with high dispersion Echelle
172 optics at China University of Geosciences, Beijing (CUGB). The precision (1σ) based
173 on rock standards BCR-1, AGV-2 and GSR-3 is estimated as $\sim 1.5\%$ for TiO_2 , $\sim 2.0\%$
174 for P_2O_5 and better than 1% for other major oxides. And trace elements were analyzed
175 using an Agilent-7500a inductively coupled plasma mass spectrometry (ICP-MS) at
176 CUGB. The BCR-1 and BHVO-1 were used to calibrate the elemental concentrations
177 of the samples. The analytical precision was generally better than 5% for most trace
178 elements, 10-13% for Cu, Sc, Nb, Er, Th, and U, and 10-15% for Ta, Tm and Gd. Full
179 sample preparation techniques and other details are described by Song *et al.* (2010).

180 Results are listed in Table 3.

181

182 3.3. Sr-Nd-Hf isotopes

183 The whole-rock Sr-Nd-Hf isotopic composition of twenty-two samples were
184 determined at GPMR. Sr and Nd isotopic ratios were measured on a Thermo Finnigan
185 Triton Ti thermal ionization mass spectrometer (TIMS), Analytical details are given in
186 Gao *et al.* (2004). And Hf isotopic analysis was conducted using a multi-collector
187 inductively coupled plasma mass spectrometer (MC-ICP-MS) with a Thermo Neptune
188 Plus system. The procedures of chemical separation and analysis are following Yang *et*

189 *al.* (2010b). The isotopic data are presented in Table 4.

190

191 **4. Results**

192 *4.1. Zircon U-Pb ages*

193 Zircons from all the analytical samples are transparent, light brown euhedral
194 columnar crystals. They have faint (Fig. 3a), oscillatory (Fig. 3b, c, f, g), sector (Fig.
195 3e) and transitional (Fig. 3d) zoning, which is consistent with a magmatic origin (Corfu
196 *et al.*, 2003). The LA-ICP-MS U–Pb analysis gave variable Th (101-4815ppm) and U
197 (115-8483ppm) concentrations with Th/U ratios of 0.15-1.21, which are of a magmatic
198 origin (Hoskin & Schaltegger, 2003). Thus, the youngest U-Pb age group of the zircons
199 represents the crystallization age. All the data are given in Appendix A.

200 Zircons from sample AKDL12-01 and NSK12-09 yield weighted mean $^{206}\text{Pb}/^{238}\text{U}$
201 ages of $251.4 \pm 6.8\text{Ma}$ (MSWD=4.1, n=9) and $247.6 \pm 4.8\text{Ma}$ (MSWD=10.3, n=10),
202 respectively. And zircons from sample BLX12-09 and BLX12-03 yield concordia ages
203 of $250.5 \pm 0.74\text{Ma}$ (MSWD=3.5, n=16) and $247.8 \pm 2.1\text{Ma}$ (MSWD=1.12, n=13),
204 respectively. Inherited /Captured zircon cores plotted along the concordia yield age
205 group of $\sim 900\text{Ma}$ and $\sim 500\text{-}300\text{Ma}$ (Figs. 3a-d), closing to the age of crust basement
206 of the EKOB (Xiaomiao Formation) and later metamorphism as well as anatexis event
207 (Wang *et al.*, 2004). Zircons from sample HYC12-01 and HXNC12-01 yield weighted
208 mean $^{206}\text{Pb}/^{238}\text{U}$ ages of $245.5 \pm 9.2\text{Ma}$ (MSWD=9.6, n=8) and $237.8 \pm 3.8\text{Ma}$
209 (MSWD=4.6, n=15), and the concordia age $227.1 \pm 0.74\text{Ma}$ (MSWD=0.84, n=17) is

given by zircons from sample BLXD12-06, respectively. Our new data can be considered as approximating the emplacement ages of the granitoids in the EKOB, which, together with the high-quality zircon U-Pb ages reported in the recent literature (summarized in Table 1), indicate that these granitoids continually formed from early Triassic (~251 Ma) to late Triassic (~214 Ma).

215

216 *4.2. Major and trace elements*

217 The Triassic granitoids from the EKOB show high SiO₂ (60.06-75.83 wt.%) and
218 low Na₂O+K₂O (4.72-9.17 wt.%) with a relatively narrow compositional range from
219 diorite, granodiorite to granite in total alkali (Na₂O+K₂O)-SiO₂ space (Fig. 4a). In the
220 (Na₂O+K₂O-CaO) against SiO₂ discrimination diagram (Fig. 4b), most of these rocks
221 are restricted in the calc-alkalic field with scattered ones falling in the alkali-calcic and
222 calcic fields. The early Triassic granitoids varying from low-K calc-alkaline series to
223 high-K calc-alkaline series (K₂O = 0.47-4.47 wt.%). Comparatively, the middle Triassic
224 granitoids fall in the calc-alkaline and high-K calc-alkaline fields (K₂O = 1.18-4.94
225 wt.%). The late Triassic granitoids with higher K₂O of 2.59-5.55 wt.% belong to high-
226 K calc-alkaline and shoshonite series (Fig. 4c). They are all weakly metaluminous to
227 peraluminous (A/NK = 1.11-2.34, A/CNK = 0.87-1.13), which are equivalent to I-type
228 granitoids with only two samples straddling the I- to S-type boundary (Fig. 4d). As
229 expected, these Triassic granitoids display decreasing trends in major elements with
230 increasing SiO₂ (Fig. 5).

231 The Triassic granitoids invariably show enrichment of light rare earth elements
232 (LREE) with $(\text{La/Yb})_{\text{N}}$ of 6.37-49.23. Most samples show significant negative Eu
233 anomalies with a few showing weak positive Eu anomalies ($\text{Eu}/\text{Eu}^* = 0.09$ -1.47; Table
234 2 and Figs. 6a-c). They share similar primitive mantle normalized patterns with
235 enrichment in Rb (although one sample of the early Triassic granitoids is distinct), K,
236 Pb and depletion in Nb, Ta, P, Ti, resembling the composition of the bulk continental
237 crust (BCC; Rudnick & Gao, 2003), as well as variable Sr anomalies (Sr/Sr^* of 0.19-
238 1.06 for T₁ granitoids, 0.08-1.98 for T₂ granitoids and 0.03-1.11 for T₃ granitoids)
239 (Table 2).

240

241 4.3. Sr-Nd-Hf isotopes

242 Bulk-rock Sr-Nd-Hf isotopic data (Table 3) are plotted in Figures 7-10. Three
243 samples (AKDL12-04, DGL12-05 and DGL12-07) gives very high $^{87}\text{Sr}/^{86}\text{Sr}$ (0.7555-
244 0.8559) because of the high Rb/Sr (13.8-24.9) (Table 3), due to significant plagioclase-
245 dominated (and alkali feldspars to some content) fractional crystallization, resembling
246 peralkaline rhyolites (Shao *et al.*, 2015). Such high Rb/Sr resulting in high radiogenic
247 ^{87}Sr ingrowth, which makes the calculated $I_{\text{Sr}}(t)$ unreliable (Wu *et al.*, 2000).
248 Eliminating these samples with inaccurate I_{Sr} (not shown in the Figs.7-10), the Triassic
249 granitoids have variable I_{Sr} of 0.7067-0.7327. The $\varepsilon_{\text{Nd}(t)}$ and $\varepsilon_{\text{Hf}(t)}$ of all samples range
250 from -9.21 to -1.66 and -7.50 to 3.59, respectively.

251

252 **5. Discussion**

253 5.1 FC (fractional crystallization) or AFC (assimilation and fractional crystallization)

254 The data shown in SiO₂-variation diagrams (Fig. 5) are to a first-order consistent
255 with varying extent of fractional crystallization of hornblende, plagioclase, Fe-Ti
256 oxides and apatite. However, these trends are also consistent with modal variations of
257 these phases in the samples although the depletion in P, Ti, Sr and Eu emphasizes the
258 significance of fractional crystallization.

259 Crustal assimilation and fractional crystallization (AFC) of mantle-derived mafic
260 magma generally produce continuous compositions from basaltic to felsic and typical
261 linear trends between SiO₂ and I_{Sr} / ε_{Nd(t)}, because of high ⁸⁷Sr/⁸⁶Sr and low ¹⁴³Nd/¹⁴⁴Nd
262 in the upper continental crust. There is a narrow spectrum of rock composition (Fig. 4a)
263 and lack of linear trends in plots of SiO₂ against I_{Sr} and ε_{Nd(t)} (Fig. 7a-b). Additionally,
264 they have lower K₂O/Na₂O than the melts produced by assimilation experiments
265 simulating the reaction between basalts and felsic pelitic gneiss in the crust (Castro,
266 2001) (Fig. 7d). These suggest that the AFC from common parental mantle-derived
267 mafic magmas is unlikely an important mechanism for the Triassic granitoids from the
268 EKOB. Alternatively, they show variable REE patterns and a wide range of bulk-rock
269 Sr-Nd-Hf isotopic compositions from the early to late Triassic (Figs. 6a-c and 7a-c),
270 which may indicate different sources and/or different petrogenetic processes. However,
271 any petrogenetic model must satisfy the observation that the Triassic granitoids have
272 hybrid mantle-crust geochemical signatures, as evidenced by their Sr-Nd-Hf isotopic

273 compositions (Figs. 8, 9 and 10).

274

275 5.2. Petrogenesis

276 S-, I-, A- and M-type granites are widely used classifications on the basis and
277 sources and petrogenesis (Collins *et al.*, 1982; Whalen *et al.*, 1987; Chappell & White,
278 2001). Chemically, the Triassic granitoids from the EKOB have relatively low A/CNK
279 values (<=1.1; Figure 4d) and amphiboles and biotite are common (Fig. 2), which accord
280 with features of I-type granites (Chappell & White, 2001). Therefore, the Triassic
281 granitoids from the EKOB are I-type granites, to be exact, they are calc-alkaline I-type
282 granitoids as shown in Figure 4. Such rocks can form by (1) crustal assimilation and
283 fractional crystallization of mantle-derived mafic magma (AFC) (Chen & Arakawa,
284 2005; De Souza *et al.*, 2007); (2) partial melting of crustal materials at deep or shallow
285 (Laurent *et al.*, 2014; Liu *et al.*, 2015); (3) hybridization between mantle-derived mafic
286 magmas and crustal melts (Dong *et al.*, 2011); (4) partial melting of remained basaltic
287 ocean crust with sediment mélange (Castro *et al.*, 2010; Huang *et al.*, 2014; Zhang *et*
288 *al.*, 2016; Shao *et al.*, 2017; Kong *et al.*, 2017).

289

290 5.2.1. Petrogenesis of the early Triassic (~ 251-248 Ma) granitoids

291 The early Triassic granitoids (T_1 , ~ 251-248 Ma) are enriched in Rb, K, Pb and
292 depleted in Nb, Ta, Sr, P and Ti, which resembles the composition of the bulk
293 continental crust (BCC; Fig. 6d). Abnormally, the sample (AKDL12-03) displays strong

negative Rb anomaly due to its extremely low content of Rb (7.7 ppm). It may be attributed to some possible reasons such as strong alteration. The T₁ granitoids have higher I_{Sr} (0.7067-0.7148), negative $\epsilon_{Nd(t)}$ (-7.32 to -1.66) and negative to positive $\epsilon_{Hf(t)}$ (-5.11 to 3.59) than the mature continental crust ($[^{87}\text{Sr}/^{86}\text{Sr}]_i = 0.73802$, $\epsilon_{Nd(t)} = -17.0$, $\epsilon_{Hf(t)} = -15.5$; Shao *et al.*, 2017), suggesting significant mantle contribution (or juvenile crustal material) in terms of isotopes. The Hf isotopic data of the T₁ granitoids and the other Kunlun Triassic granitoids (Fig. 9; Ding *et al.*, 2015; Huang *et al.*, 2014; Xia *et al.*, 2015; Zhang *et al.*, 2016; Shao *et al.*, 2017) are also indicative of significant mantle contribution. To produce such andesitic to felsic BCC-like magmas with mantle signature, it requires a basaltic source plus continental materials mentioned above. As shown in many previous studies, the A'nyemaqen Ocean (the north branch of the Paleo-Tethys Ocean recorded in the EKOB; Jiang *et al.*, 1992) had closed and recorded a syn-collisional setting in the early Triassic (Huang *et al.*, 2014; Shao *et al.*, 2017), in which setting the potential basaltic source may be the arc crust (island arc basalt, IAB) or the subducted ocean crust (mid-ocean ridge basalt, MORB). Higher Sr/Sr* values of IAB (~ 2.72) than that of BCC (0.933) and MORB (~ 0.1-2.0) have been used by Niu and co-authors (Niu and O'Hara, 2009; Niu *et al.* (2013) to argue against IAB for the source of T₁ granitoids ($\text{Sr/Sr}^* = 0.19-1.06$). Therefore, the basaltic end-member for the source of T₁ granitoids is most probably supplied by the subducted ocean crust (i.e. MORB). Note that their flat HREE (mean $[\text{Dy/Yb}]_N = 1.1$, the same as BCC) patterns and constant $(\text{Ce/Yb})_N$ with decrease Yb_N (Fig. 6a, d), requires melting under amphibolite

315 facies conditions (< 50 km; without garnet signature). Additionally, the trace element
316 patterns, as well as the isotopic composition, especially the Nd-Hf isotopes of the T_1 (~
317 251-248 Ma) granitoids are consistent with the I-type syn-collisional granitoids derived
318 from melting of subducted oceanic crust with terrigenous sediments of upper
319 continental crust origin (Figs. 7a, b, c and 8, 9,10). Partial melting of the ocean crust
320 produces felsic melts and the ocean crust derived from the mantle not long ago imparts
321 the mantle isotopic signature (Niu *et al.*, 2013). Meanwhile, the addition of terrigenous
322 sediment can explain the crustal signatures of the T_1 granitoids. Many lines of evidence
323 above suggest the T_1 (~ 251-248 Ma) granitoids are derived from partial melting of
324 remaining fragments of the subducted A'nyemaqen ocean crust with recycled
325 terrigenous sediment under amphibolite facies conditions. The underthrusting cold
326 Anyemaqen Ocean crust evolves along a high T/P geothermal path and has longer time
327 to absorb heat from the prior hot active continental margin. The highly hydrated ocean
328 crust (along with terrigenous sediments) begins to melt when it reaches the hydrous
329 basaltic solidus (<700 °C) under amphibolite conditions (see details in Mo *et al.*, 2008;
330 Niu *et al.*, 2013). The melts subsequently underwent plagioclase-controlled
331 fractionation within crustal reservoirs supported by relatively large decrease in Al_2O_3 ,
332 CaO (Fig. 5b, e) and Sr , Eu (Fig. 7e, f) with small increase in SiO_2 . It should be noted
333 that the initial isotopic ratio (I_{Sr} , $\varepsilon_{\text{Nd}}(t)$ and $\varepsilon_{\text{Hf}}(t)$) variations within individual outcrops
334 largely reflect small scale isotopic heterogeneity due to incomplete homogenization of
335 melts affected by crustal assimilation or modal variation or both. This is because

336 granitoid magmas under sub-liquidus conditions are “crystal mashes”, complete
337 homogenization is thus restricted by the efficient diffusion (Ramos and Reid, 2005).
338 Inherited/captured zircon cores plotted along the concordia yield age group of ~900Ma
339 and ~ 500-300Ma (Figs. 3a-d), closing to the age of crust basement of the EKOB
340 (Xiaomiao Formation) and later metamorphism (Wang *et al.*, 2004), implying that they
341 were involved in the ~250 Ma magmatism. Terrigenous sediments melted alongside
342 oceanic crust also result in the isotope heterogeneity.

343 Studies of the Linzizong volcanic succession (LVS) in southern Tibet have
344 testified that juvenile continental crust is produced via partial melting of the ocean crust
345 under the amphibolite facies conditions and preserved as ‘net crust growth’ in the
346 collision zones (Niu *et al.*, 2013; Mo *et al.*, 2008; Niu and O'Hara, 2009). The syn-
347 collisional East Kunlun granitoids provide more geochemical and isotopic data to
348 support this hypothesis. Firstly, the bulk compositions of granitoids are similar to the
349 bulk continental crust with almost identical Nb-Ta-Ti and Sr and Eu depletion (Fig. 6a,
350 d). Secondly, the whole rock Sr-Nd-Hf isotopes can be explained by partial melting of
351 subducted Paleo-Tethyan MORB with terrigenous sediment addition in the melting
352 region under the amphibolite-facies conditions (see above). Though the granitoids in
353 the EKOB have relatively unradiogenic Nd isotope ($\epsilon_{Nd}(t)<0$) compared to the LVS,
354 they have high $\epsilon_{Hf}(t)$ values (up to 3.59), which is the more convincing evidence that
355 they are juvenile crust newly formed from ocean crust melting with inherited mantle
356 isotopic signatures and crustal/sediment contribution.

357

358 5.2.2. Petrogenesis of the middle (~ 247-238 Ma) and late Triassic (~ 234-214 Ma)

359 granitoids

360 Since the middle Triassic (T_2 , ~ 247-238 Ma) and late Triassic (T_3 , ~ 234-214 Ma)

361 granitoids display similar trace elemental and isotopic features (Figs. 6-10), we hence

362 discuss them together here. The T_2 and T_3 granitoids have almost consistent mean

363 values of $\varepsilon_{\text{Nd(t)}}$ (-5.83 [T_2], -5.97 [T_3]) and $\varepsilon_{\text{Hf(t)}}$ (-3.52 [T_2], -3.58 [T_3]), indicating a

364 similar source. REE patterns of the T_2 and T_3 granitoids show weakly concave upward

365 between middle and heavy REEs (Fig. 6b-c), suggesting amphibole as a residual phase

366 in the source due to its high partition coefficients for middle to heavy REEs, especially

367 the highest D(Dy) in intermediate to felsic melts (Rollinson, 1993). Meanwhile, the

368 multi-element patterns of the T_2 and T_3 granitoids show obvious decrease from Dy to

369 Yb (Fig. 6e-f), which imply garnet may also be a residual phase in their source ($K_d^{\text{Grt/L}} = 39.9$; Arth, 1976).

370 The existence of garnet as a residual phase may be responsible for

371 the adakitic signature (Castillo, 2012) of the T_2 and T_3 granitoids. Most of the T_2 and

372 T_3 granitoids have relatively high Sr/Y and La/Yb, plotting in the field restricted to

373 adakite (Figs. 7h-i). Petrogenesis of adakitic rocks are considered as follows: (1) related

374 to the melting of subducted slab directly or indirectly (Martin *et al.*, 2005); (2) melting

375 of the mafic lower continental crust (e.g. Atherton & Petford, 1993; Goss & Kay, 2009);

376 (3) high pressure fractionation of garnet-bearing normal arc magma (Macpherson *et al.*,

377 2006). Their high $^{87}\text{Sr}/^{86}\text{Sr}$ (0.7107-0.7523), low $^{143}\text{Nd}/^{144}\text{Nd}$ (0.5120-0.5123) are not a

typical signature of melting of subducted slab (Castillo, 2012). Considering the lithostratigraphic records, these granitoids cannot be interpreted as product of arc magmatism (*Jiang et al.*, 1992). Therefore, partial melting of the lower continental crust may account for the origin of the granitic rock. First, the T₂ and T₃ granitoids from the EKOB have high (La/Yb)_N (Fig. 6b,c) and high K₂O/ Na₂O ratios (Fig. 7d), which are consistent with the composition of adakitic rocks inferred to be derived from partial melting of the lower continental crust. Second, the T₂ and T₃ granitoids from the EKOB have Sr (⁸⁷Sr/⁸⁶Sr, 0.7107-0.7523), Nd ($\varepsilon_{\text{Nd(t)}}$, -5.83 [T₂], -5.97 [T₃]) and Hf ($\varepsilon_{\text{Hf(t)}}$, -3.52 [T₂], -3.58 [T₃]) isotopes similar to the T₁ grantoids (Fig. 8, 9), are likely indicative of significant juvenile mafic continental crust. Meanwhile, according to the mass balance, the T₂ and T₃ granitoids requires some input of mature crustal material (Fig.10b). Finally, the overlapping Sr-Nd-Hf isotope compositions of the T₂ and T₃ granitoids are consistent with the I-type granitoids derived from the lower continental crust as well as the sub-volcanic rocks derived from crust-mantle mixing (Fig. 8; *Zhang et al.*, 2012; *Ding et al.*, 2011; *Hu et al.*, 2016), which also suggest the T₂ and T₃ granitoids could be produced by melting of the juvenile mafic lower continental crust, mixing with the upper continental crust components during ascent. In which a newly lower crust thickened (probably ~ 50km with lowest temperature gradient of 20°C km⁻¹; Atherton & Petford, 1993) by underplating under garnet stability conditions played an important role, resulting in adakitic features of the T₂ and T₃ granitoids. They likely experienced fractional crystallization of plagioclase (Figs. 5b, e; 7e-f). Furthermore, high partition

399 coefficient of Sc but low value of Th in biotite will result in lower Sc/Th of residual
400 melts during biotite fractionation (Bea *et al.*, 1994). Negative correlation between
401 Sc/Th and SiO₂ denotes the biotite fractionation in T₂ and T₃ granitoids (Fig. 7g). In
402 fact, melting the lower crust clearly need a heat source from below. Post-collisional
403 setting of the late Triassic has been widely accepted in the EKOB (e.g. Pan *et al.*, 2012;
404 Wang *et al.*, 2014a). Many mechanisms such as mantle plume (Chung & Jahn, 1995),
405 slab break-off (Maury *et al.*, 2000) or convective lithosphere removal (Hoernle *et al.*,
406 2006) can cause asthenospheric upwelling, decompression melting, triggering crustal
407 melting. Accordingly, we prefer the more reasonable post-collisional extension and
408 related orogenic collapse for inducing asthenosphere upwelling, and then leading to
409 mafic lower crust melting to form T₂ and T₃ granitoids. The age range of the T₃
410 granitoids (~234-214 Ma) are similar to the late Triassic mafic dikes and felsic volcanic
411 rocks (228-218 Ma) associated with post-collisional extension in the EKOB (Hu *et al.*,
412 2016) suggest these post-collisional magmatism is an important tectono-magmatic
413 event which has influenced both the lower crust and the upper mantle. More importantly,
414 the identical genetic link between T₂ and T₃ granitoids has pushed this event back to
415 ~247 Ma, that is the EKOB had transformed to post-collisional setting since the middle
416 Triassic (~247 Ma).

417
418 5.3 An integrated model from syn-collisional to post-collisional settings
419 Our integrate model implies a process of partial melting of the subducted

420 A'nyemaqen ocean crust with terrestrial sediments in a syn-collisional setting (~ 251-
421 248 Ma) and partial melting of juvenile mafic lower crust mixing with the upper crust
422 components in a post-collisional setting (~ 247-214 Ma). Figure 10 shows mixing
423 calculations for the Triassic granitoids in the EKOB. The T₁ (~ 251-248 Ma) granitoids
424 represent mixing of at least ~ 50% A'nyemaqen MORB (Guo *et al.*, 2007) and ~ 50%
425 terrigenous sediments represented by the Jinshuikou granites derived from the
426 Proterozoic basement of Qaidam terrane (Yu *et al.*, 2005). Comparably, the T₂ (~ 247-
427 238 Ma) and T₃ (~ 234-214 Ma) granitoids are best explained as hybrid magmas of ~
428 55% juvenile mafic lower crust (Hu *et al.*, 2016) and ~ 45% upper continental crust
429 materials (also logically represented by the Jinshuikou granitoids; Yu *et al.*, 2005).
430 Melting of A'nyemaqen ocean crust fragments with recycled terrigenous sediment
431 under amphibolite facies conditions resulted in the T₁ granitoids with mantle signatures
432 (e.g. $\epsilon_{\text{Hf(t)}}$ > 0), which share similar compositions with the BCC. This process added a
433 net flux of juvenile dioritic to granitic materials to the continental crust, pointing to the
434 significance of the oceanic crust melting for continental crust accretion (Fig.11a). T₂
435 and T₃ granitoids are associated with post-collisional magmatism involving
436 participation of juvenile continental crust. Asthenosphere upwelling and decompression
437 melting would provide heat for juvenile mafic lower crust melting, then mixing with
438 upper crust during post-collisional extension (Fig.11b). These hypotheses are
439 conceptually important for understanding the origin of the juvenile crust and continental
440 crustal growth through magmatism from syn-collisional to post-collisional settings.

441 Further research is needed to test these hypotheses.

442

443 **6. Conclusion**

444 1. The zircon U-Pb dating yields ages of ~ 251-248 Ma, ~ 247-238 Ma to ~ 234-214
445 Ma for the granitoids of the East Kunlun Orogenic Belt. These age data, together with
446 the literature data, suggest that the granitoids are products of syn-collisional (~ 251-248
447 Ma) and post-collisional (~ 247-238 Ma to ~ 234-214 Ma) magmatism during or shortly
448 after the closure of the A'nyemaqen Ocean.

449 2. The early Triassic (~ 251-248 Ma) granitoids are best explained by partial melting of
450 the subducted A'nyemaqen ocean crust fragments with recycled terrigenous sediment
451 under amphibolite facies conditions. The contribution of the ocean crust at least ~ 50%
452 to the parental melts of the T₁ granitoids, which subsequently underwent fractionation.

453 3. The middle (~ 247-238 Ma) and late (~ 234-214 Ma) Triassic granitoids with adakitic
454 features could be produced by melting of the juvenile mafic lower continental crust,
455 mixing with the upper continental crust components during ascent, in which the relative
456 proportion of juvenile mafic lower crust may be up to ~ 55% to their parental melts.

457 This process is more reasonably associated with post-collisional extension for inducing
458 asthenosphere upwelling, leading to mafic lower crust melting to form the granitoids.

459 4. The early Triassic (~ 251-248 Ma) granitoids with mantle signatures (e.g. $\epsilon_{\text{Hf(t)}}$ > 0)
460 as well as BCC-like compositions represent a net flux of juvenile dioritic to granitic
461 materials adding to the continental crust, pointing to the significance of melting of

462 ocean crust for continental crust accretion in the EKOB. And the identical genetic link
463 between T₂ (~ 247-238 Ma) and T₃ (~ 234-214 Ma) granitoids means the EKOB had
464 transformed to post-collisional setting since the middle Triassic (~ 247 Ma).

465

466

467 **Acknowledgements**

468 We thank Pengyuan Guo, Pu Sun, Zhenxing Hu, Jinju Liu and Huixia Cui for help in
469 the field, and Lian Zhou for assistance with isotope analysis. We also thank Professor
470 Michael Roden and two anonymous reviewers for their constructive comments and
471 suggestions on the manuscript improvement. This work was supported by grants from
472 Chinese Academy of Sciences, regional and local authorities (Shandong Province and
473 City of Qingdao, U1606401), Natural Foundation of Shandong Province
474 (ZR2018BD020), Qingdao National laboratory of ocean sciences and Technology
475 (2015ASKJ03) and National Natural Science Foundation of China (41630968,
476 91014003, 41803028, 91958215) and the 111 Project of China (B118048).

477

478 **References**

- 479 Atherton, M. P. & Petford, N. (1993). Generation of sodium-rich magmas from newly
480 underplated basaltic crust. *Nature* **362**, 144-146.
- 481 Ba, J., Chen, N. S., Wang, Q. Y., Wang, X. Y., Zhang, L. & Wang, S. Q. (2012). Nd-Sr-
482 Pb isotopic compositions of cordierite granite on southern margin of the qaidam

- 483 block, NW China, and constraints on its petrogenesis, tectonic affinity of source
484 region and tectonic implications. *Earth Science-Journal of China University of*
485 *Geosciences*, 80-92.
- 486 Bacon, C. R. & Druitt, T. H. (1988). Compositional evolution of the zoned calc-alkaline
487 magma chamber of Mount Mazama, Crater Lake, Oregon. *Contributions to*
488 *Mineralogy and Petrology* **98**, 224-256.
- 489 Bea, F., Pereira, M. D. & Stroh, A. (1994). Mineral/leucosome trace-element
490 partitioning in a peraluminous migmatite (a laser ablation-ICP-MS study).
491 *Chemical Geology* **117**, 291-312.
- 492 Bian, Q. T., Yin, L. M., Sun, S. F., Luo, X. Q., Pospelov, I., Astrakhantsev, O. & Chamov,
493 N. (2001). Discovery of Ordovician acritarchs in Buqingshan ophiolite complex,
494 East Kunlun Mountains and its significance. *Chinese Science Bulletin* **46**, 341-
495 345.
- 496 Castillo, P. R. (2012). Adakite petrogenesis. *Lithos* **134**, 304-316.
- 497 Castro, A. (2001). Plagioclase morphologies in assimilation experiments. Implications
498 for disequilibrium melting in the generation of granodiorite rocks. *Mineralogy*
499 *and Petrology* **71**, 31-49.
- 500 Castro, A., Gerya, T., García-Casco, A., Fernández, C., Díaz-Alvarado, J., Moreno-
501 Ventas, I. & Löw, I. (2010). Melting relations of MORB-sediment mélange in
502 underplated mantle wedge plumes; implications for the origin of cordilleran-type
503 batholiths. *Journal of Petrology* **51**, 1267-1295.

- 504 Chappell, B. W. & White, A. J. R. (2001). Two contrasting granite types: 25 years later.
- 505 *Australian Journal of Earth Sciences* **48**, 489-499.
- 506 Chen, B. & Arakawa, Y. (2005). Elemental and Nd-Sr isotopic geochemistry of
- 507 granitoids from the West Junggar foldbelt (NW China), with implications for
- 508 Phanerozoic continental growth. *Geochimica et Cosmochimica Acta* **69**, 1307-
- 509 1320.
- 510 Chen, H. W., Luo, Z. H., Mo, X. X., Zhang, X. T., Wang, J. & Wang, B. Z. (2006).
- 511 SHRIMP ages of Keyakedengtage complex in the East Kunlun Mountains and
- 512 their geological implications. *Acta Petrologica ET Mineralogica* **25**, 25-32.
- 513 Chen, N. S., Sun, M., Wang, Q. Y., Zhao, G. C., Chen, Q. & Shu, G. M. (2007). EMP
- 514 chemical ages of monazites from Central Zone of the eastern Kunlun Orogen:
- 515 Records of multi-tectonometamorphic events. *Chinese Science Bulletin* **52**, 2252-
- 516 2263.
- 517 Chen, N. S., Sun, M., Zhang, K. X. & Zhu, Y. H. (2001). ^{40}Ar - ^{39}Ar and U-Pb ages of
- 518 metadiorite from the East Kunlun Orogenic Belt: Evidence for Early-Paleozoic
- 519 magmatic zone and excess argon in amphibole minerals. *Chinese Science Bulletin*
- 520 **46**, 330-333.
- 521 Chen, Y. X., Pei, X. Z., Li, R. B., Liu, Z. Q., Li, Z. C., Zhang, X. F., Chen, G. C., Liu,
- 522 Z. G., Ding, S. P. & Guo, J. F. (2011). Zircon U-Pb age of Xiaomiao Formation
- 523 of Proterozoic in the eastern section of the East Kunlun Orogenic Belt.
- 524 *Geoscience* **25**, 510-521.

- 525 Chung, S. L. & Jahn, B. M. (1995). Plume-lithosphere interaction in generation of the
526 Emeishan flood basalts at the Permian-Triassic boundary. *Geology* **23**, 889-892.
- 527 Collins, W., Beams, S., White, A. & Chappell, B. (1982). Nature and origin of A-type
528 granites with particular reference to southeastern Australia. *Contributions to
529 Mineralogy and Petrology* **80**, 189-200.
- 530 Corfu, F., Hanchar, J. M., Hoskin, P. W. O. & Kinny, P. (2003). Atlas of Zircon Textures.
531 *Reviews in Mineralogy and Geochemistry* **53**, 469-500.
- 532 De Souza, Z. S., Martin, H., Peucat, J.-J., De Sá, E. F. J. & Macedo, M. H. D. F. (2007).
533 Calc-alkaline magmatism at the Archean-Proterozoic transition: the Caicó
534 Complex Basement (NE Brazil). *Journal of Petrology* **48**, 2149-2185.
- 535 Ding, Q. F., Jiang, S. Y. & Sun, F. Y. (2014). Zircon U-Pb geochronology, geochemical
536 and Sr-Nd-Hf isotopic compositions of the Triassic granite and diorite dikes from
537 the Wulonggou mining area in the Eastern Kunlun Orogen, NW China:
538 Petrogenesis and tectonic implications. *Lithos* **205**, 266-283.
- 539 Ding, Q., Liu, F. & Yan, W. (2015). Zircon U-Pb geochronology and Hf isotopic
540 constraints on the petrogenesis of Early Triassic granites in the Wulonggou area
541 of the Eastern Kunlun Orogen, Northwest China. *International Geology Review*
542 **57**, 1735–1754.
- 543 Ding, S., Huang, H., Niu, Y. L., Zhao, Z. D., Yu, X. H. & Mo, X. X. (2011).
544 Geochemistry, geochronology and petrogenesis of East Kunlun high Nb-Ta
545 rhyolites. *Acta Petrologica Sinica* **27**, 3603-3614.

- 546 Dong, Y. P., Zhang, G. W., Neubauer, F., Liu, X. M., Hauzenberger, C., Zhou, D. W. &
547 Li, W. (2011). Syn-and post-collisional granitoids in the Central Tianshan orogen:
548 geochemistry, geochronology and implications for tectonic evolution. *Gondwana*
549 *Research* **20**, 568-581.
- 550 Frost, B. R., Barnes, C. G., Collins, W. J., Arculus, R. J., Ellis, D. J. & Frost, C. D.
551 (2001). A geochemical classification for granitic rocks. *Journal of Petrology* **42**,
552 2033-2048.
- 553 Gao, S., Rudnick, R. L., Yuan, H. L., Liu, X. M., Liu, Y. S., Xu, W. L., Ling, W. L.,
554 Ayers, J., Wang, X. C. & Wang, Q. H. (2004). Recycling lower continental crust
555 in the North China craton. *Nature* **432**, 892-897.
- 556 Goss, A. R. & Kay, S. M. (2009). Extreme high field strength element (HFSE) depletion
557 and near-chondritic Nb/Ta ratios in Central Andean adakite-like lavas ($\sim 28^\circ$ S, \sim
558 68° W). *Earth and Planetary Science Letters* **279**, 97-109.
- 559 Guo, A. L., Zhang, G. W., Sun, Y. G., Cheng, S. Y. & Qiang, J. (2007). Sr-Nd-Pb
560 isotopic geochemistry of late-Paleozoic mafic volcanic rocks in the surrounding
561 areas of the Gonghe basin, Qinghai province and geological implications. *Acta
562 Petrologica Sinica* **23**.
- 563 Hoernle, K., White, J. D. L., van den Bogaard, P., Hauff, F., Coombs, D. S., Werner, R.,
564 Timm, C., Garbe-Schönberg, D., Reay, A. & Cooper, A. F. (2006). Cenozoic
565 intraplate volcanism on New Zealand: Upwelling induced by lithospheric
566 removal. *Earth and Planetary Science Letters* **248**, 350-367.

- 567 Hoskin, P. W. O. & Schaltegger, U. (2003). The composition of zircon and igneous and
568 metamorphic petrogenesis. Washington, DC, ETATS-UNIS: Mineralogical
569 Society of America, 36.
- 570 Hu, Y., Niu, Y. L., Li, J. Y., Ye, L., Kong, J. J., Chen, S., Zhang, Y. & Zhang, G. R.
571 (2016). Petrogenesis and tectonic significance of the Late Triassic mafic dikes
572 and felsic volcanic rocks in the East Kunlun Orogenic Belt, Northern Tibet
573 Plateau. *Lithos* **245**, 205-222.
- 574 Huang, H., Niu, Y. L., Nowell, G., Zhao, Z. D., Yu, X. H., Zhu, D. C., Mo, X. X. &
575 Ding, S. (2014). Geochemical constraints on the petrogenesis of granitoids in the
576 East Kunlun Orogenic belt, northern Tibetan Plateau: Implications for continental
577 crust growth through syn-collisional felsic magmatism. *Chemical Geology* **370**,
578 1-18.
- 579 Irving, A. J. & Frey, F. A. (1978). Distribution of trace elements between garnet
580 megacrysts and host volcanic liquids of kimberlitic to rhyolitic composition.
581 *Geochimica et Cosmochimica Acta* **42**, 771-787.
- 582 Jiang, C. F., Yang, J. S., Feng, B. G., Zhu, Z. Z., Zhao, M., Chai, Y. C., Shi, X. D., Wang,
583 H. D. & Hu, J. Q. (1992). Opening-closing tectonics of Kunlun Mountains. *Series*
584 *of geological memoirs* **5**, 1-224.
- 585 Kong, J.J., Niu, Y.L., Duan, M., Zhang, Y., Hu, Y., Li, J.Y. & Chen, S. (2017).
586 Petrogenesis of Luchuba and Wuchaba granitoids in western Qinling:
587 Geochronology and geochemical evidence. *Mineralogy and Petrology* **111**, 887-

- 588 908.
- 589 Laurent, A., Janoušek, V., Magna, T., Schulmann, K. & Míková, J. (2014). Petrogenesis
590 and geochronology of a post-orogenic calc-alkaline magmatic association: the
591 Žulová Pluton, Bohemian Massif. *Journal of GEosciences*, 415-440.
- 592 Li, L., Dong, F. C., Yang, Y. Q., Zhu, Z. X., Jiang, H. B. & Xin, J. (2012). The Petrology
593 and Geochemistry of Ophiolites from Central Kunlun. *Xinjiang Geology* **30**, 19-
594 25.
- 595 Liu, C. D., Mo, X. X., Luo, Z. H., Yu, X. H., Chen, H. W., Li, S. W. & Zhao, X. (2004).
596 Mixing events between the crust- and mantle-derived magmas in eastern kunlun:
597 Evidence from zircon SHRIMP II chronology. *Chinese Science Bulletin* **49**, 828-
598 834.
- 599 Liu, Y. S., Hu, Z. C., Zong, K. Q., Gao, C. G., Gao, S., Xu, J. & Chen, H. H. (2010).
600 Reappraisal and refinement of zircon U-Pb isotope and trace element
601 analyses by LA-ICP-MS. *Chinese Science Bulletin* **55**, 1535-1546.
- 602 Liu, Z., Jiang, Y. H., Jia, R. Y., Zhao, P. & Zhou, Q. (2015). Origin of Late Triassic high-
603 K calc-alkaline granitoids and their potassic microgranular enclaves from the
604 western Tibet Plateau, northwest China: Implications for Paleo-Tethys evolution.
605 *Gondwana Research* **27**, 326-341.
- 606 Ludwig, K. R. (2012). User's manual for Isoplot version 3.75-4.15: a geochronological
607 toolkit for Microsoft. *Excel Berkley Geochronological Center Special
608 Publication*, No.5.

- 609 Luo, B. J., Zhang, H. F., Xu, W. C., Guo, L., Pan, F. B. & Yang, H. (2015). The Middle
610 Triassic Meiwu Batholith, West Qinling, Central China: Implications for the
611 Evolution of Compositional Diversity in a Composite Batholith. *Journal of*
612 *Petrology*, egv032.
- 613 Macpherson, C. G., Dreher, S. T. & Thirlwall, M. F. (2006). Adakites without slab
614 melting: high pressure differentiation of island arc magma, Mindanao, the
615 Philippines. *Earth and Planetary Science Letters* **243**, 581-593.
- 616 Maniar, P. D. & Piccoli, P. M. (1989). Tectonic discrimination of granitoids. *Geological*
617 *Society of America Bulletin* **101**, 635-643.
- 618 Martin, H., Smithies, R. H., Rapp, R., Moyen, J. F. & Champion, D. (2005). An
619 overview of adakite, tonalite–trondhjemite–granodiorite (TTG), and sanukitoid:
620 relationships and some implications for crustal evolution. *Lithos* **79**, 1-24.
- 621 Maury, R. C., Fourcade, S., Coulon, C., Bellon, H., Coutelle, A., Ouabadi, A., Semroud,
622 B., Megartsi, M. h., Cotten, J. & Belanteur, O. (2000). Post-collisional Neogene
623 magmatism of the Mediterranean Maghreb margin: a consequence of slab
624 breakoff. *Comptes Rendus de l'Académie des Sciences-Series IIA-Earth and*
625 *Planetary Science* **331**, 159-173.
- 626 Middlemost, E. A. (1994). Naming materials in the magma/igneous rock system. *Earth-*
627 *Science Reviews* **37**, 215-224.
- 628 Mo, X. X., Luo, Z. H., Deng, J. F., Yu, X. H., Liu, C. D., Chen, H. W., Yuan, W. M. &
629 Liu, Y. H. (2007). Granitoids and Crustal Growth in the East-Kunlun Orogenic

- 630 Belt. *Geological Journal of China Universities* **13**, 403-414.
- 631 Mo, X. X., Niu, Y. L., Dong, G. C., Zhao, Z. D., Hou, Z. Q., Zhou, S. & Ke, S. (2008).
- 632 Contribution of syncollisional felsic magmatism to continental crust growth: a
633 case study of the Paleogene Linzizong volcanic succession in southern Tibet.
- 634 *Chemical Geology* **250**, 49-67.
- 635 Niu, Y. L. & O'Hara, M. J. (2009). MORB mantle hosts the missing Eu (Sr, Nb, Ta and
636 Ti) in the continental crust: New perspectives on crustal growth, crust–mantle
637 differentiation and chemical structure of oceanic upper mantle. *Lithos* **112**, 1-17.
- 638 Niu, Y. L., Zhao, Z. D., Zhu, D. C. & Mo, X. X. (2013). Continental collision zones are
639 primary sites for net continental crust growth — A testable hypothesis. *Earth-
640 Science Reviews* **127**, 96-110.
- 641 Pan, G. T., Wang, L. Q., Li, R. S., Yuan, S. H., Ji, W. H., Yin, F. G., Zhang, W. P. &
642 Wang, B. D. (2012). Tectonic evolution of the Qinghai-Tibet Plateau. *Journal of
643 Asian Earth Sciences* **53**, 3-14.
- 644 Haidong, R. , Tao, W. , Lei, Z. , Xiaoxia, W. , He, H. , & Chengyou, F. (2016). Ages,
645 sources and tectonic settings of the triassic igneous rocks in the easternmost
646 segment of the east kunlun orogen, central china. *Acta Geologica Sinica - English
647 Edition* **90**(2), 641-668.
- 648 Ramos, F.C., Reid, M.R. (2005). Distinguishing melting of heterogeneous mantle
649 sources from crustal contamination: insights from Sr isotopes at the Phenocryst
650 Scale, Pisgah Crater, California. *Journal of Petrology* **46**, 999-1012

- 651 Rickwood, P. C. (1989). Boundary lines within petrologic diagrams which use oxides
652 of major and minor elements. *Lithos* **22**, 247-263.
- 653 Rollinson, H. (1993). Using Geochemical Data: Evaluation, Interpretation, Presentation.
654 Longman, New York.
- 655 Rudnick, R. L. & Gao, S. (2003). Composition of the continental crust. *Treatise on
656 Geochemistry* **3**, 1-64.
- 657 Shao, F. L., Niu, Y. L., Regelous, M. & Zhu, D. C. (2015). Petrogenesis of peralkaline
658 rhyolites in an intra-plate setting: Glass House Mountains, southeast Queensland,
659 Australia. *Lithos* **216**, 196-210.
- 660 Shao, F. , Niu, Y. , Liu, Y. , Chen, S. , Kong, J. , & Duan, M . (2017). Petrogenesis of
661 triassic granitoids in the east kunlun orogenic belt, northern tibetan plateau and
662 their tectonic implications. *Lithos* **282-283**, 33-44.
- 663 Song, S. G., Su, L., Li, X. H., Zhang, G. B., Niu, Y. L. & Zhang, L. F. (2010). Tracing
664 the 850-Ma continental flood basalts from a piece of subducted continental crust
665 in the North Qaidam UHPM belt, NW China. *Precambrian Research* **183**, 805-
666 816.
- 667 Sun, S.-s. & McDonough, W. F. (1989). Chemical and isotopic systematics of oceanic
668 basalts: implications for mantle composition and processes. *Geological Society,
669 London, Special Publications* **42**, 313-345.
- 670 Sun, Y., Pei, X. Z., Ding, S. P., Li, R. B., Feng, J. Y., Zhang, Y. F., Li, Z. C., Chen, Y.
671 X., Zhang, X. F. & Chen, G. C. (2009). Halagatu magma mixing granite in the

- 672 East Kunlun Mountains-Evidence from Zircon U-Pb dating. *Acta Geologica*
- 673 *Sinica* **83**, 1000-1010.
- 674 Taylor, S. R. (1967). The origin and growth of continents. *Tectonophysics* **4**, 17-34.
- 675 Wang, B. Z., Chen, J., Luo, Z. H., Chen, F. B., Wang, T. & Guo, G. E. (2014a). Spatial
676 and temporal distribution of Late Permian-Early Jurassic intrusion assemblages
677 in eastern Qimantag, East Kunlun, and their tectonic settings. *Acta Petrologica*
- 678 *Sinica* **30**, 3213-3228.
- 679 Wang, C., Liu, L., Xiao, P. X., Cao, Y. T., Yu, H. Y., Meert, J. G. & Liang, W. T. (2014b).
- 680 Geochemical and geochronologic constraints for Paleozoic magmatism related to
681 the orogenic collapse in the Qimantagh-South Altyn region, northwestern China.
- 682 *Lithos* **202–203**, 1-20.
- 683 Wang, G. C., Wang, Q. H., Ran, P. & Zhu, Y. H. (2004). Zircon SHRIMP ages of
684 Precambrian metamorphic basement rocks and their tectonic significance in the
685 eastern Kunlun Mountains, Qinghai Province, China. *Dixue Qianyuan(Earth*
686 *Science Frontiers)* **11**, 481-490.
- 687 Wang, G. C., Wei, Q. R., Jia, C. X., Zhang, K. X., Li, D. W., Zhu, Y. H. & Xiang, S. Y.
688 (2007). Some ideas of Precambrian geology in the East Kunlun, China.
689 *Geological Bulletin of China* **26**, 929-937.
- 690 Whalen, J. B., Currie, K. L. & Chappell, B. W. (1987). A-type granites: geochemical
691 characteristics, discrimination and petrogenesis. *Contributions to Mineralogy and*
692 *Petrology* **95**, 407-419.

- 693 Wiedenbeck, M., Alle, P., Corfu, F., Griffin, W. L., Meier, M., Oberli, F., Quadt, A. v.,
- 694 Roddick, J. C. & Spiegel, W. (1995). Three natural zircon standards for U - Th -
- 695 Pb, Lu - Hf, trace element and REE analyses. *Geostandards Newsletter* **19**, 1-23.
- 696 Wu, F. Y., Jahn, B. M., Wilde, S. & Sun, D. Y. (2000). Phanerozoic crustal growth: U -
- 697 Pb and Sr-Nd isotopic evidence from the granites in northeastern China.
- 698 *Tectonophysics* **328**, 89-113.
- 699 XACGS. (2009). Geological map of Kunlun mountain and its adjacent area, Scale 1:
- 700 1000,000. Xi'an Center of Geological Survey, China Geological Survey.
- 701 Xia, R., Wang, C., Qing, M., Li, W., Carranza, E.J.M., Guo, X., Ge, L. & Zeng, G.
- 702 (2015). Zircon U-Pb dating, geochemistry and Sr-Nd-Pb-Hf-O isotopes for the
- 703 Nan'getan granodiorites and mafic microgranular enclaves in the East Kunlun
- 704 orogen: record of closure of the Paleo-Tethys. *Lithos* **234-235**, 47-60.
- 705 Xiong, F. H., Ma, C. Q., Jiang, H. A., Liu, B. & Huang, J. (2014). Geochronology and
- 706 geochemistry of Middle Devonian mafic dykes in the East Kunlun orogenic belt,
- 707 Northern Tibet Plateau: Implications for the transition from Prototethys to
- 708 Paleotethys orogeny. *Chemie der Erde - Geochemistry* **74**, 225-235.
- 709 Xiong, F. H., Ma, C. Q., Zhang, J. Y. & Liu, B. (2012). The origin of mafic
- 710 microgranular enclaves and their host granodiorites from East Kunlun, Northern
- 711 Qinghai-Tibet Plateau: implications for magma mixing during subduction of
- 712 Paleo-Tethyan lithosphere. *Mineralogy and Petrology* **104**, 211-224.
- 713 Xu, Z. Q., Dilek, Y., Cao, H., Yang, J. S., Robinson, P., Ma, C. Q., Li, H. Q., Jolivet,

- 714 M., Roger, F. & Chen, X. J. (2015). Paleo-Tethyan Evolution of Tibet as Recorded
715 in the East Cimmerides and West Cathaysides. *Journal of Asian Earth Sciences*
716 **105**, 320-337.
- 717 Yang, J. S., Xu, Z. Q., Ma, C. Q., Wu, C. L., Zhang, J. X., Wang, Z. Q., Wang, G. C.,
718 Zhang, H. F., Dong, Y. P. & Lai, S. C. (2010a). Compound orogeny and scientific
719 problems concerning the Central Orogenic Belt of China. *Geology in China* **37**,
720 1-11.
- 721 Yang, Y. H., Zhang, H. F., Chu, Z. Y., Xie, L. W. & Wu, F. Y. (2010b). Combined
722 chemical separation of Lu, Hf, Rb, Sr, Sm and Nd from a single rock digest and
723 precise and accurate isotope determinations of Lu–Hf, Rb–Sr and Sm–Nd isotope
724 systems using Multi-Collector ICP-MS and TIMS. *International Journal of Mass
725 Spectrometry* **290**, 120-126.
- 726 Yu, N., Jin, W., Ge, W. C. & Long, X. P. (2005). Geochemical study on peraluminous
727 granite from Jinshukou in East Kunlun. *Global Geology* **24**, 123-128.
- 728 Zhang, Y., Niu, Y. L., Hu, Y., Liu, J. J., Ye, L., Kong, J. J. & Duan, M. (2016). The
729 syncollisional granitoid magmatism and continental crust growth in the West
730 Kunlun Orogen, China—Evidence from geochronology and geochemistry of the
731 Arkarz pluton. *Lithos* **245**, 191-204.

732

733

734

Figure Captions

735

736 **Fig. 1** (a) Geological framework of the Greater Tibetan Plateau showing the major
737 tectonic units and sutures as follows (from northeast to southwest): NQS, North Qilian
738 suture; DHS, Danghe Nan Shan suture; SQS, South Qilian suture; AKMS,
739 A'nyemaqen-Kunlun-Mutztagh suture; JS, Jinsha suture; BNS, Bangong-Nujiang
740 suture; IYS, Indus-Yarlung Zangbo suture, revised after (Hu *et al.*, 2016). (b) Outline
741 of the East Kunlun Orogenic Belt with two major faults (Central Kunlun Fault and
742 South Kunlun Fault) and three magmatic zones (Northern, Middle and Southern Zone)
743 (Hu *et al.*, 2016). (c) Simplified geological map of east section of the East Kunlun
744 Orogenic Belt (modified after XACGS, 2009). U-Pb ages shown for the granitic plutons
745 are new data of this study and from the recent literature indicated with superscript
746 numerals: 1. Ding *et al.* (2014), 2. Xiong *et al.* (2012), 3. Xia *et al.* (2014a), 4. Xia *et*
747 *al.* (2014b), 5. Sun *et al.* (2009), 6. Xu *et al.* (2015) and 7. Ding *et al.* (2011).

748

749 **Fig. 2** (a, b) An outcrop of the Triassic granitoids with some mafic magmatic enclaves
750 (MMEs) from the East Kunlun Orogenic Belt. Photomicrographs of (c) biotite
751 monzogranite, (d) syenogranite, (e) biotite moyite, (f) quartz diorite, (g) granodiorite,
752 (h) granite porphyry. Kfs = potash feldspar; Qtz = quartz; Pl = plagioclase; Bt = biotite;
753 Amp = amphibole.

754

755 **Fig. 3** Concordia diagrams of zircon U-Pb age data and cathodoluminescence images

756 of representative zircons for (a) AKDL12-01, (b) BLX12-09, (c) BLX12-03, (d)
757 NSK12-09, (e) HYC12-01, (f) HXNC12-01 and (g) BLXD12-06 from the Triassic
758 granitoids in the East Kunlun Orogenic Belt. Various amounts of inherited/captured old
759 zircons of ~900 Ma and ~500-300 Ma in the early Triassic granitoids may indicate the
760 presence and involvement of old crustal materials.

761

762 **Fig. 4** Plots of (a) $\text{Na}_2\text{O}+\text{K}_2\text{O}$ against SiO_2 (Middlemost, 1994); (b) $\text{Na}_2\text{O}+\text{K}_2\text{O}-\text{CaO}$
763 against SiO_2 (Frost *et al.*, 2001); (c) K_2O against SiO_2 (Rickwood, 1989); (d) A/NK
764 (molar $\text{Al}_2\text{O}_3/[\text{Na}_2\text{O}+\text{K}_2\text{O}]$) against A/CNK (molar $\text{Al}_2\text{O}_3/[\text{CaO}+\text{Na}_2\text{O}+\text{K}_2\text{O}]$) (Maniar
765 & Piccoli, 1989; Chappell & White, 2001) for the Triassic granitoids from the East
766 Kunlun Orogenic Belt.

767

768 **Fig. 5** SiO_2 variation diagrams of the granitoids from the East Kunlun Orogenic Belt.

769

770 **Fig. 6** (a-c) Normalized rare earth element (REE) and (d-f) multi-element patterns of
771 the Triassic granitoids from the East Kunlun Orogenic Belt. Bulk continental crust
772 (BCC; Rudnick & Gao, 2003) composition is also plotted for comparison. Chondrite
773 and primitive mantle data are from Sun and McDonough (1989). The shaded fields in
774 (a) and (d) are of I-type syn-collisional granitoids derived from subducted oceanic crust
775 in the East Kunlun Orogenic Belt (Huang *et al.*, 2014).

776

777 **Fig. 7** SiO₂ variation diagrams of (a) I_{Sr}, (b) ε_{Nd(t)}, (c) ε_{Hf(t)}, (d) K₂O/Na₂O (purple filled
778 circles restricted in the purple dash line are products of the assimilation experiments
779 that simulate the reaction between basalts and felsic pelitic gneiss in the crust; (Castro,
780 2001), (e) Sr, (f) Eu and (g) Sc/Th for the Triassic granitoids from the East Kunlun
781 Orogenic Belt. Plots of (h) Sr/Y vs. Y and (i) La/Yb vs. Yb for these samples are used
782 to distinguish adakitic rocks from normal arc andesite, dacite and rhyolite (Castillo,
783 2012).

784

785 **Fig. 8** Diagrams of ε_{Nd(t)} vs. I_{Sr} (a) and ε_{Hf(t)} vs. ε_{Nd(t)} for the Triassic granitoids from the
786 East Kunlun Orogenic Belt. The field of I-type syn-collisional granitoids derived from
787 subducted oceanic crust is based on Huang *et al.* (2014) and Zhang *et al.* (2016). The
788 data for the sub-volcanic rocks derived from crust-mantle mixing are from Ding *et al.*
789 (2011) and Hu *et al.* (2016). And the I-type granitoids derived from the lower crust and
790 S-type granitoids derived from the upper crust are from Zhang *et al.* (2012) and Ba *et*
791 *al.* (2012), respectively.

792

793 **Fig. 9** The ε_{Hf(t)} vs. Ages of the Triassic granitoids of the East Kunlun orogenic belt.
794 Our new data and the literature data are indicated as the following: light blue diamonds
795 (whole rock Hf data, West Kunlun; Zhang *et al.*, 2016); green triangles (whole rock Hf
796 data, East Kunlun; Huang *et al.*, 2014); purple crosses and blue crosses (zircon Hf data,
797 East Kunlun; Ding *et al.*, 2015; Xia *et al.*, 2015) and gay circles (whole rock Hf data,

798 East Kunlun; Shao *et al.*, 2017).

799

800 **Fig. 10** Mixing trends calculated with $\epsilon_{\text{Nd(t)}}$ and $^{87}\text{Sr}/^{86}\text{Sr}$ composition for (a) the early
801 (~251-248Ma) and (b) middle (~247-238Ma) & late (~234-214Ma) Triassic granitoids
802 from the East Kunlun Orogenic Belt. T₁ granitoids could be explained by mixing
803 between A'nyemaqen MORB (average composition: $^{87}\text{Sr}/^{86}\text{Sr} = 0.707818$, $\epsilon_{\text{Nd(t)}} = 12.9$,
804 Sr = 191.5 ppm, Nd = 8.9 ppm) (Guo *et al.*, 2007) and terrigenous sediments
805 (represented by the Jinshuikou S-type granites) (average composition: $^{87}\text{Sr}/^{86}\text{Sr} =$
806 0.738282, $\epsilon_{\text{Nd(t)}} = -11.3$, Sr = 260.1 ppm, Nd = 23.3 ppm) (Yu *et al.*, 2005). Comparably,
807 T₂ & T₃ granitoids could be interpreted as mixture of Juvenile mafic lower continental
808 crust (average composition: $^{87}\text{Sr}/^{86}\text{Sr} = 0.709589$, $\epsilon_{\text{Nd(t)}} = -2.6$, Sr = 525.0 ppm, Nd =
809 33.2 ppm) (Hu *et al.*, 2016) and upper continental crust (represented by the Jinshuikou
810 S-type granites again).

811

812 **Fig. 11** Schematic illustration for the generation of the granitoids in EKOB during the
813 Triassic (modified from Shao *et al.*, 2017). See text for explanation.

Fig. 1

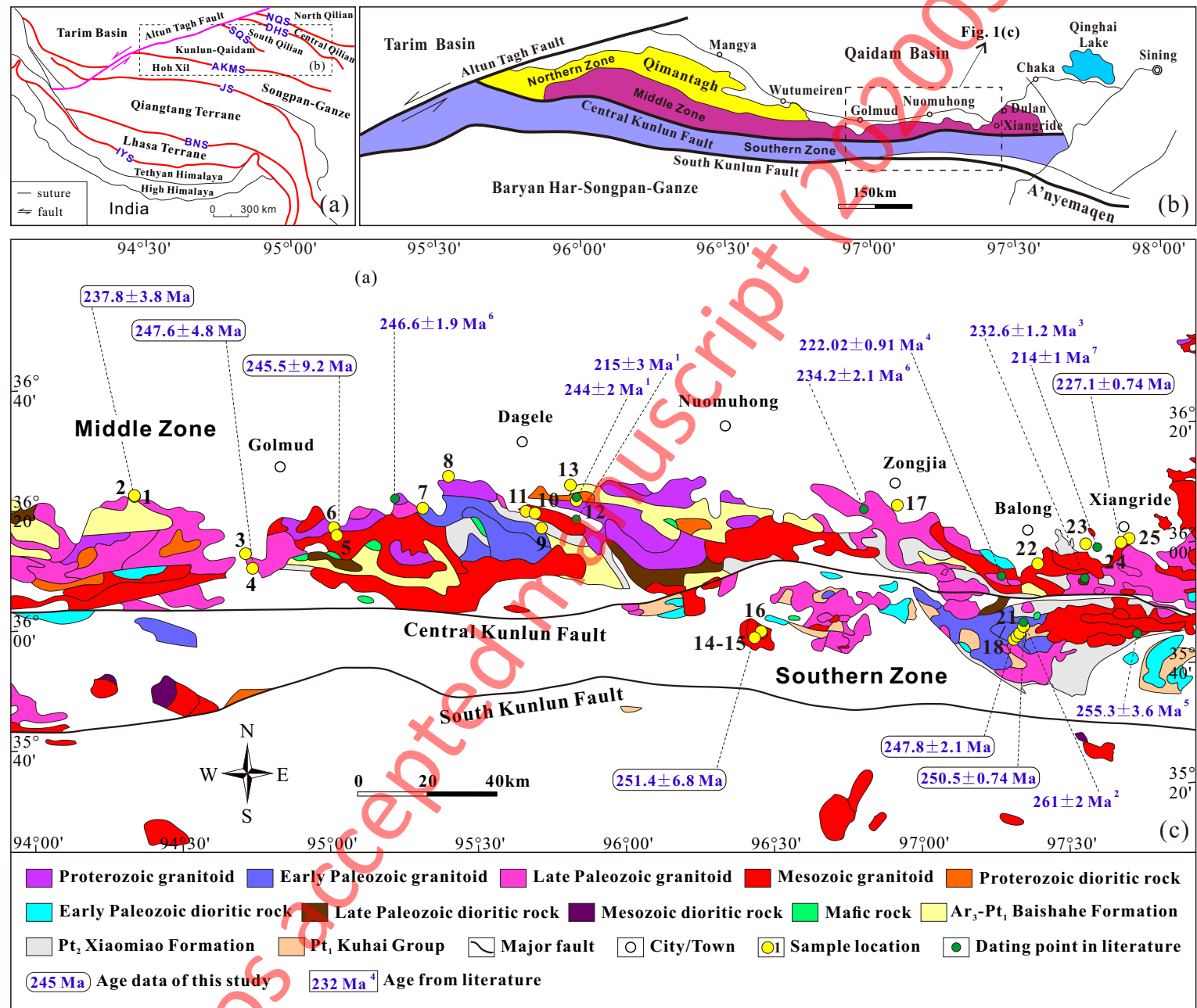
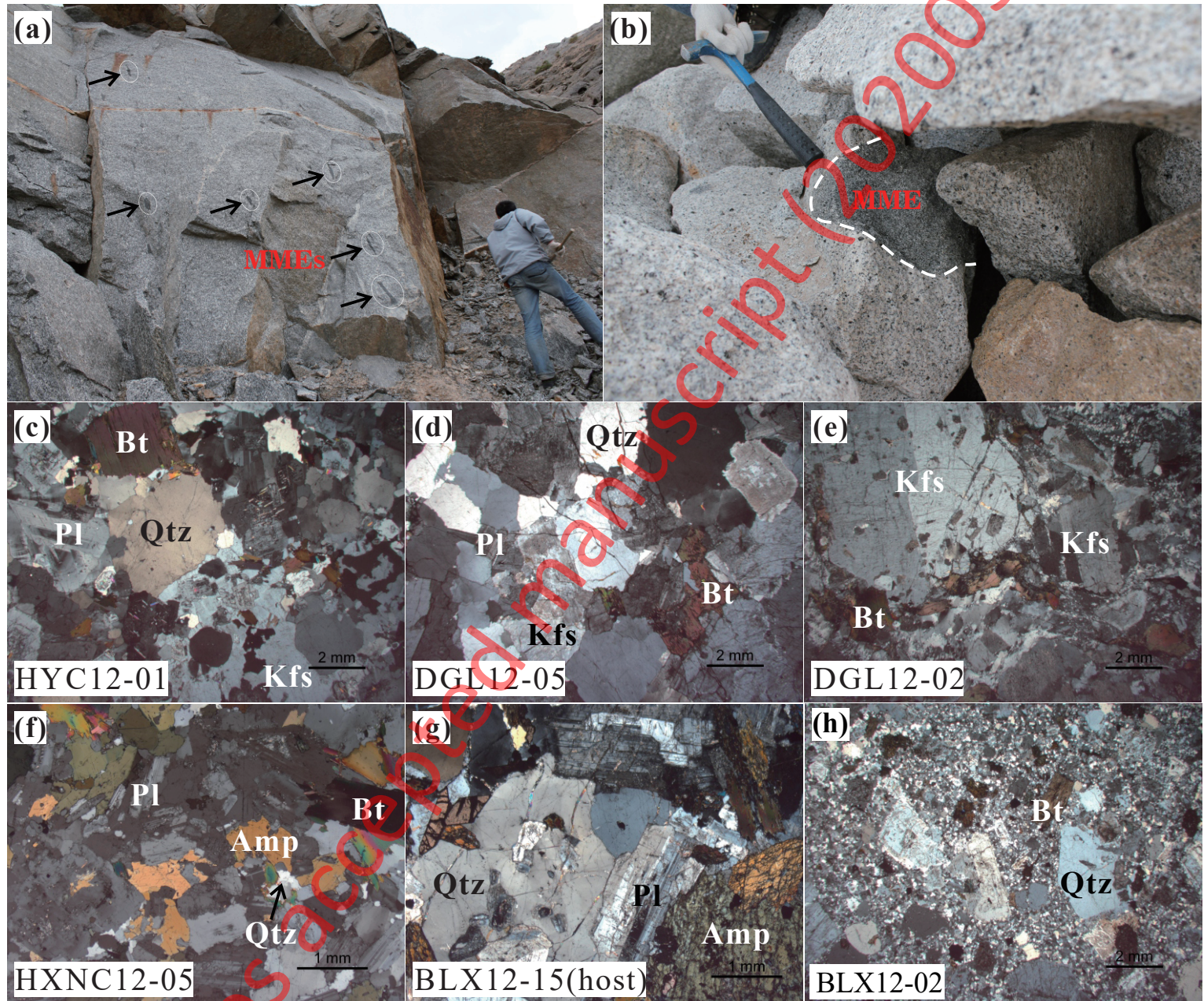


Fig. 2



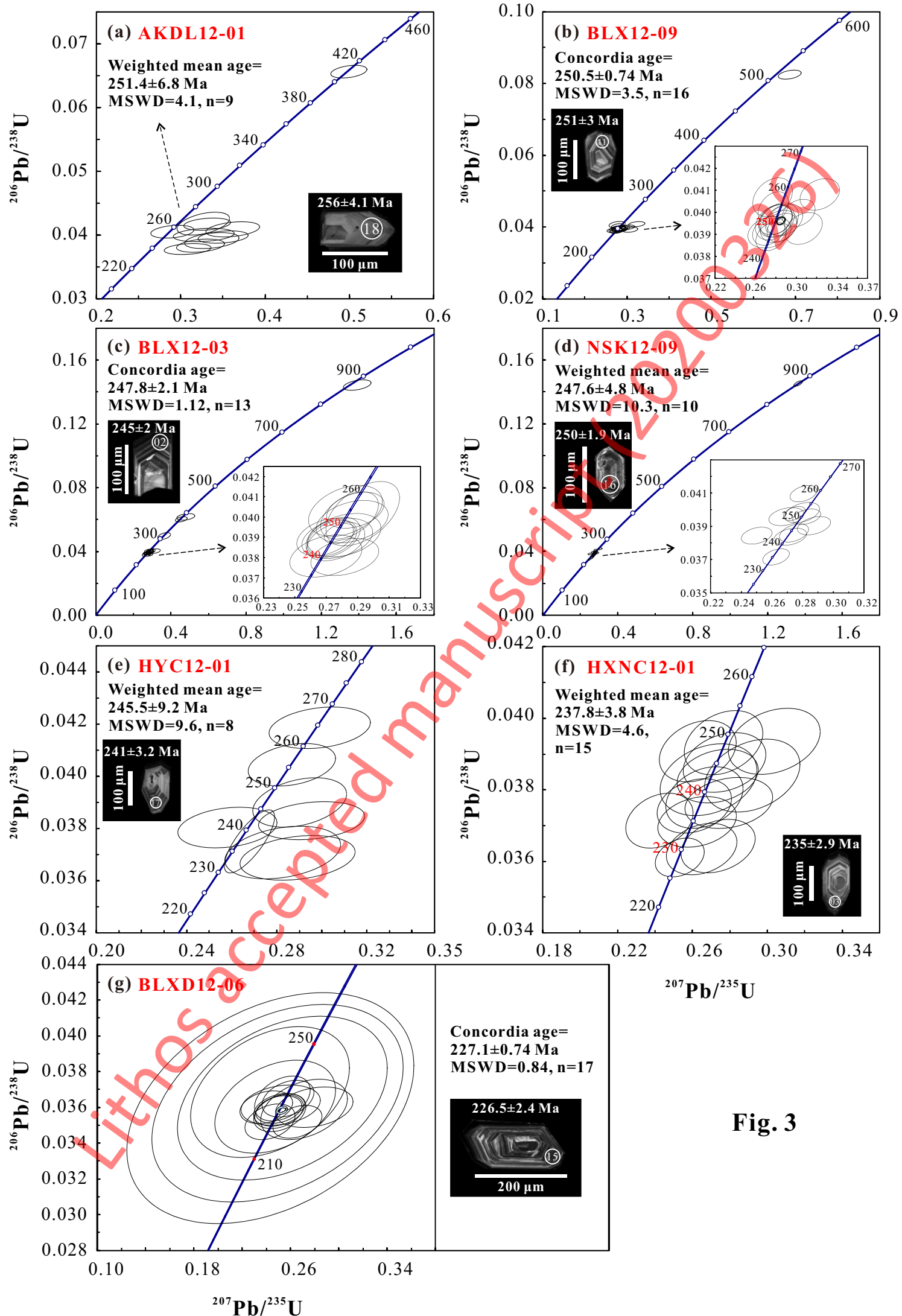


Fig. 3

Fig. 4

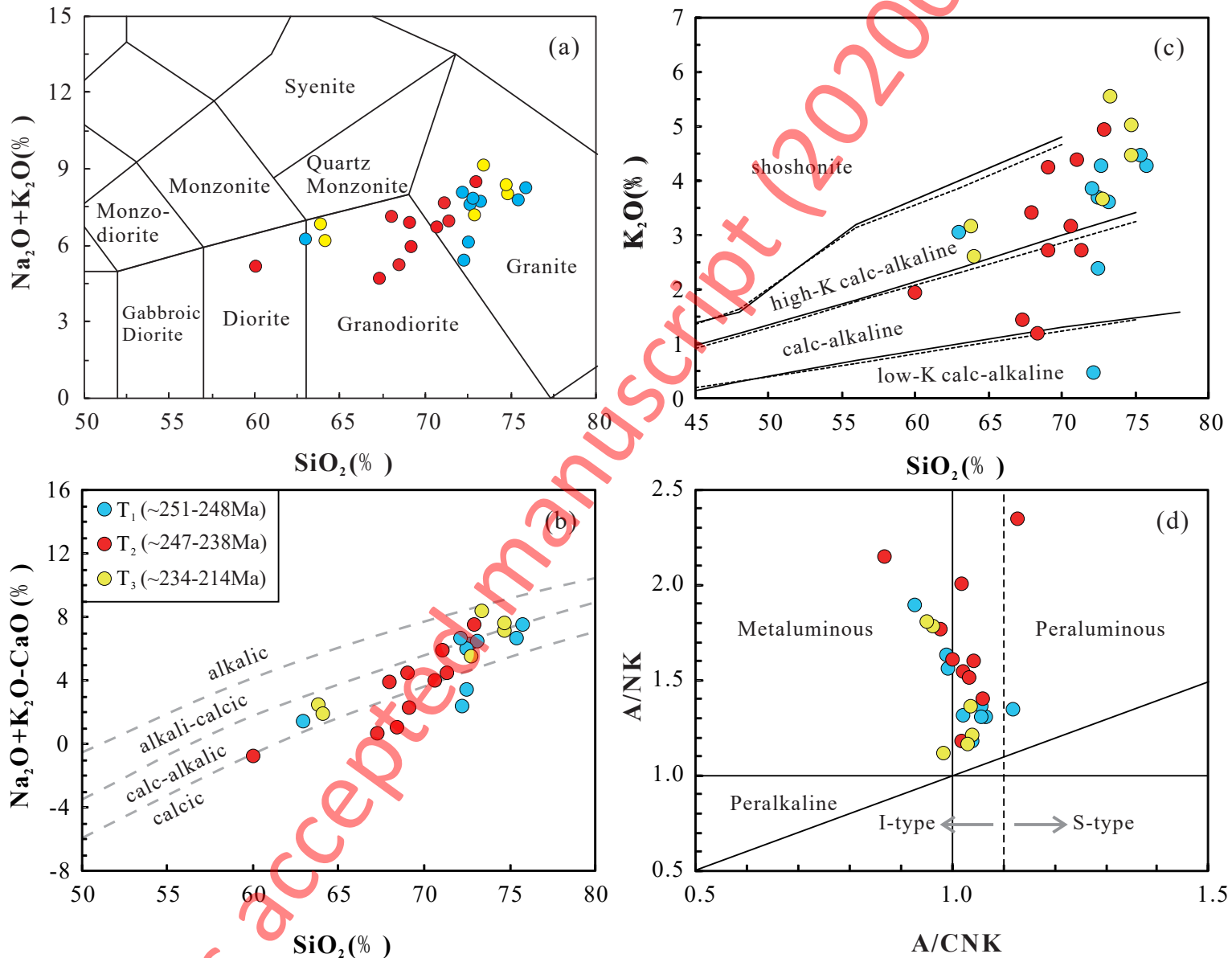


Fig. 5

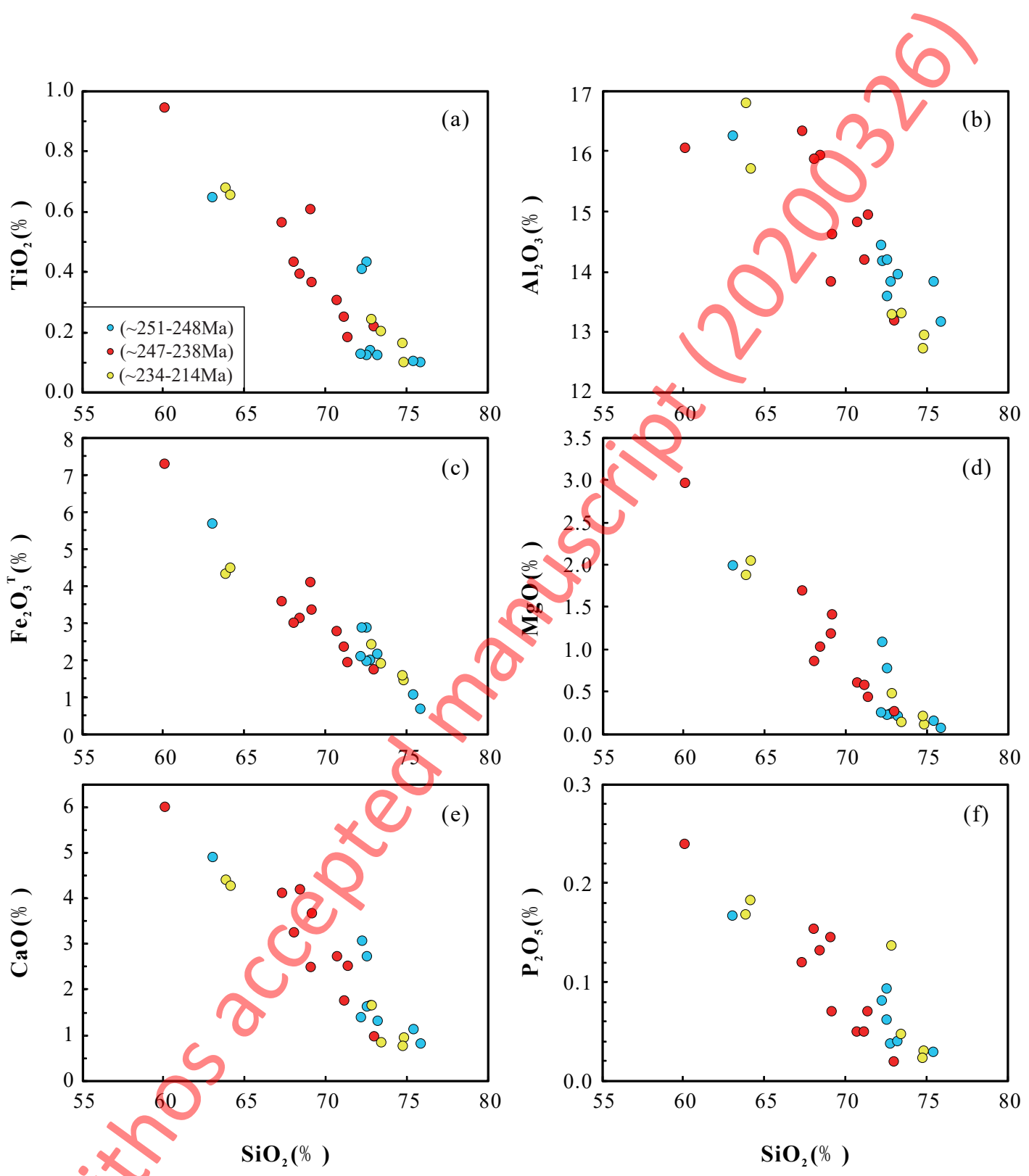


Fig. 6

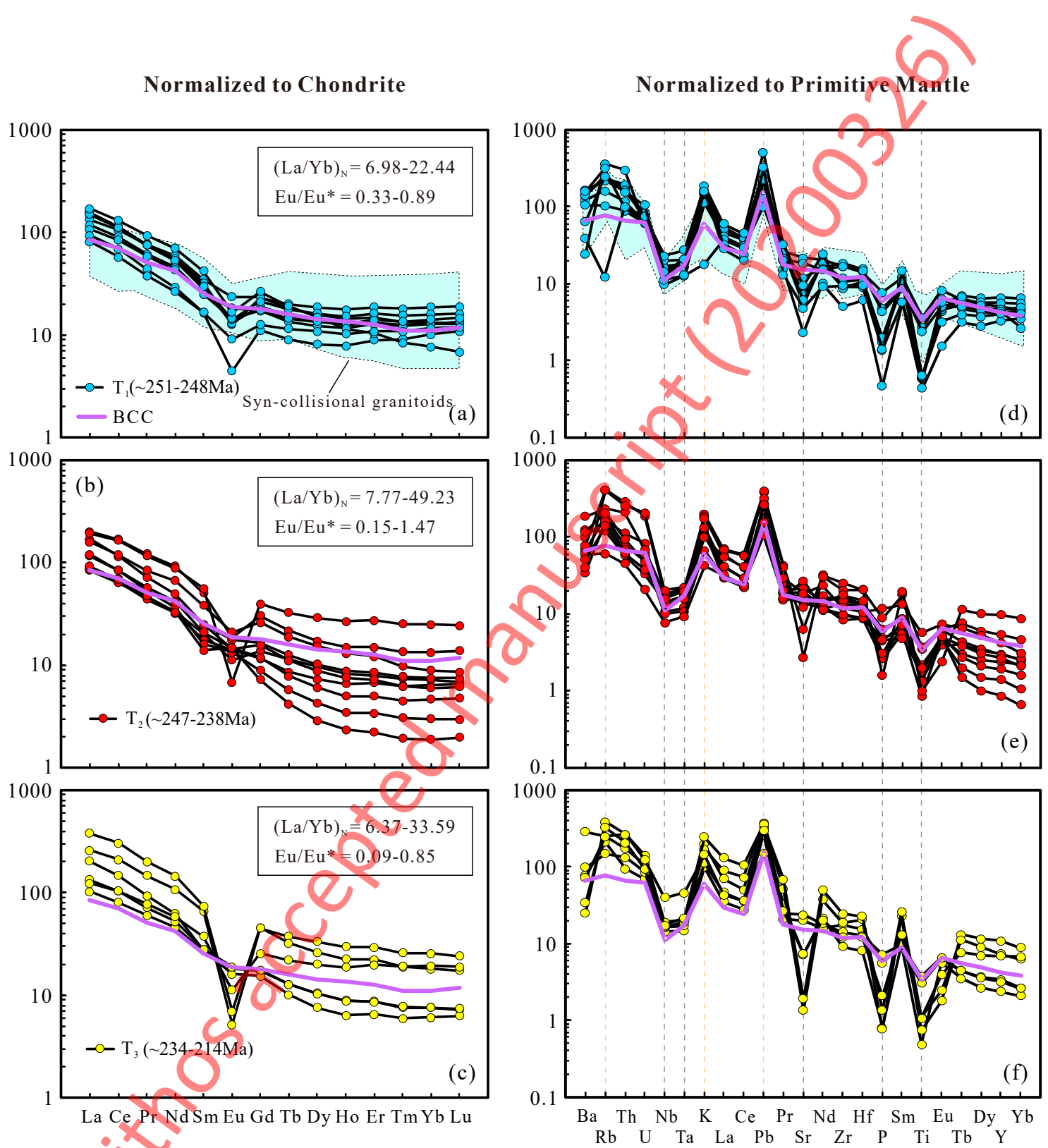


Fig. 7

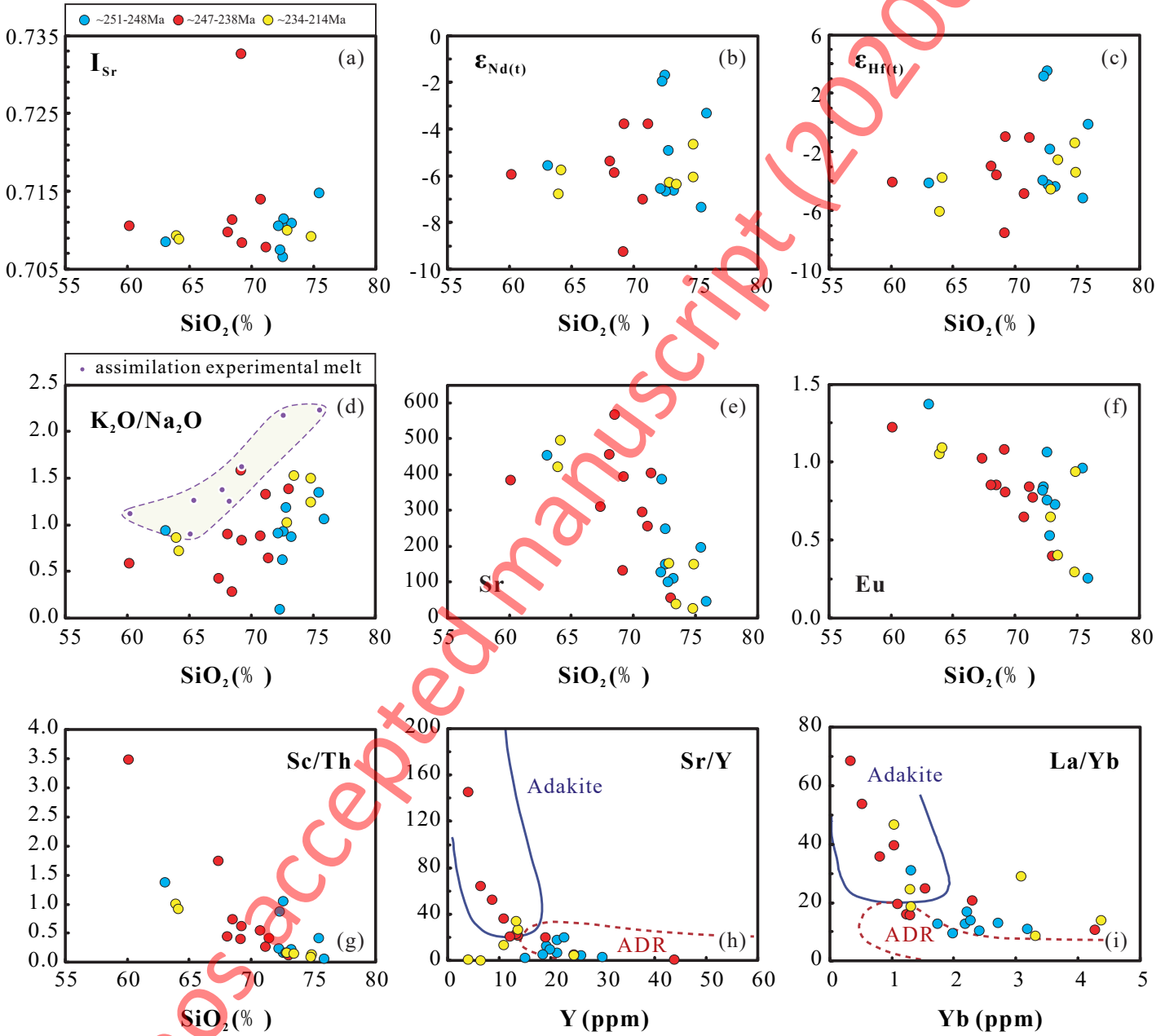
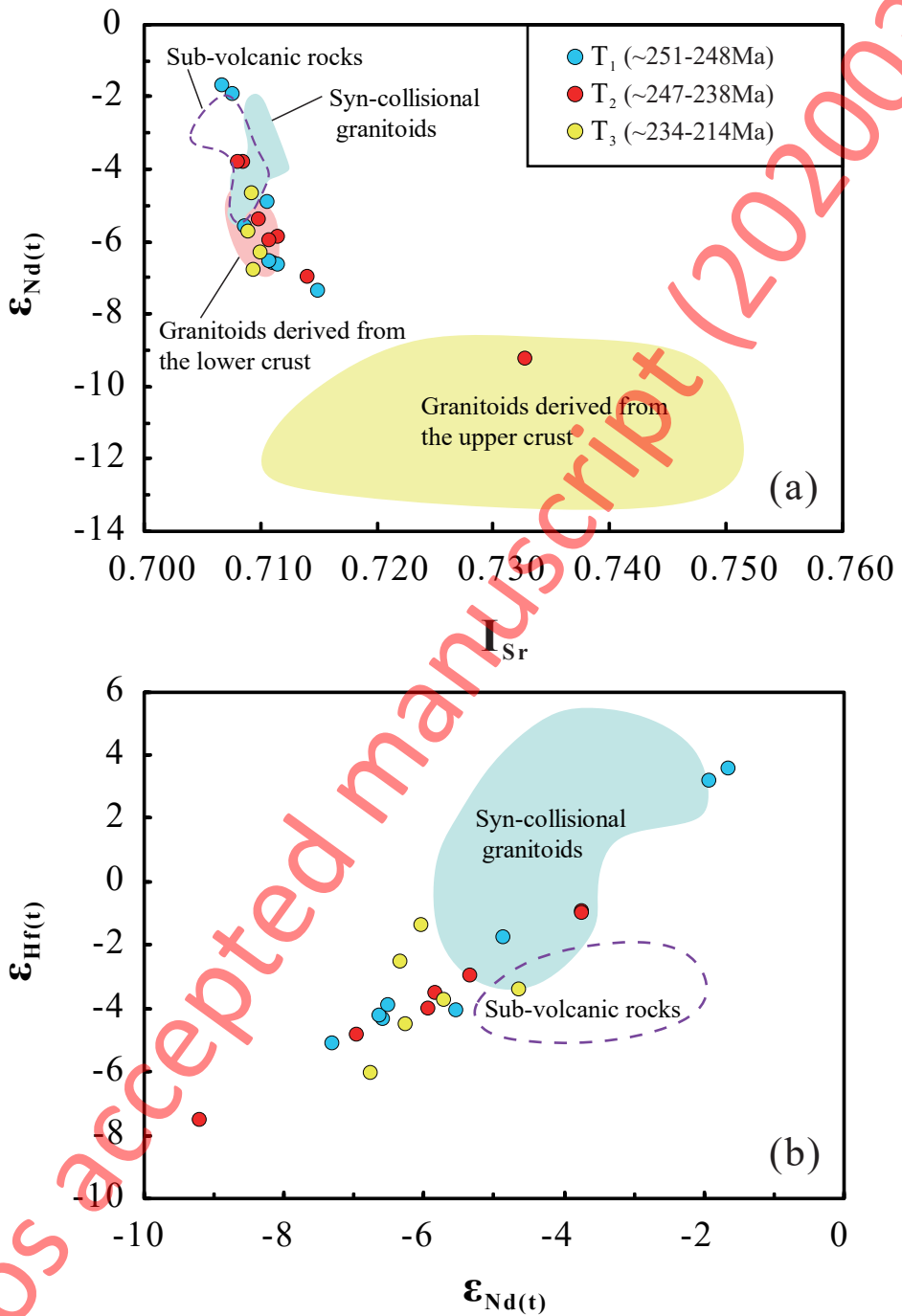
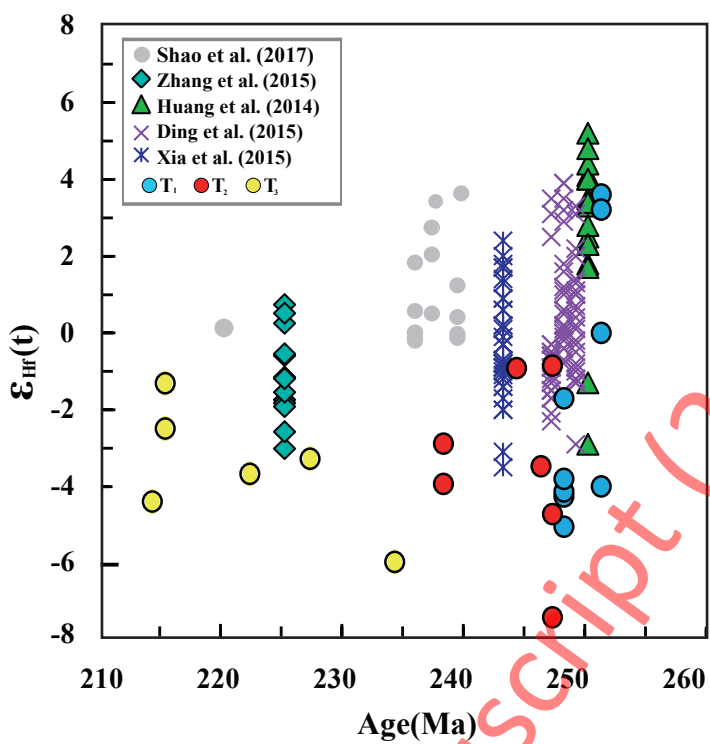


Fig. 8



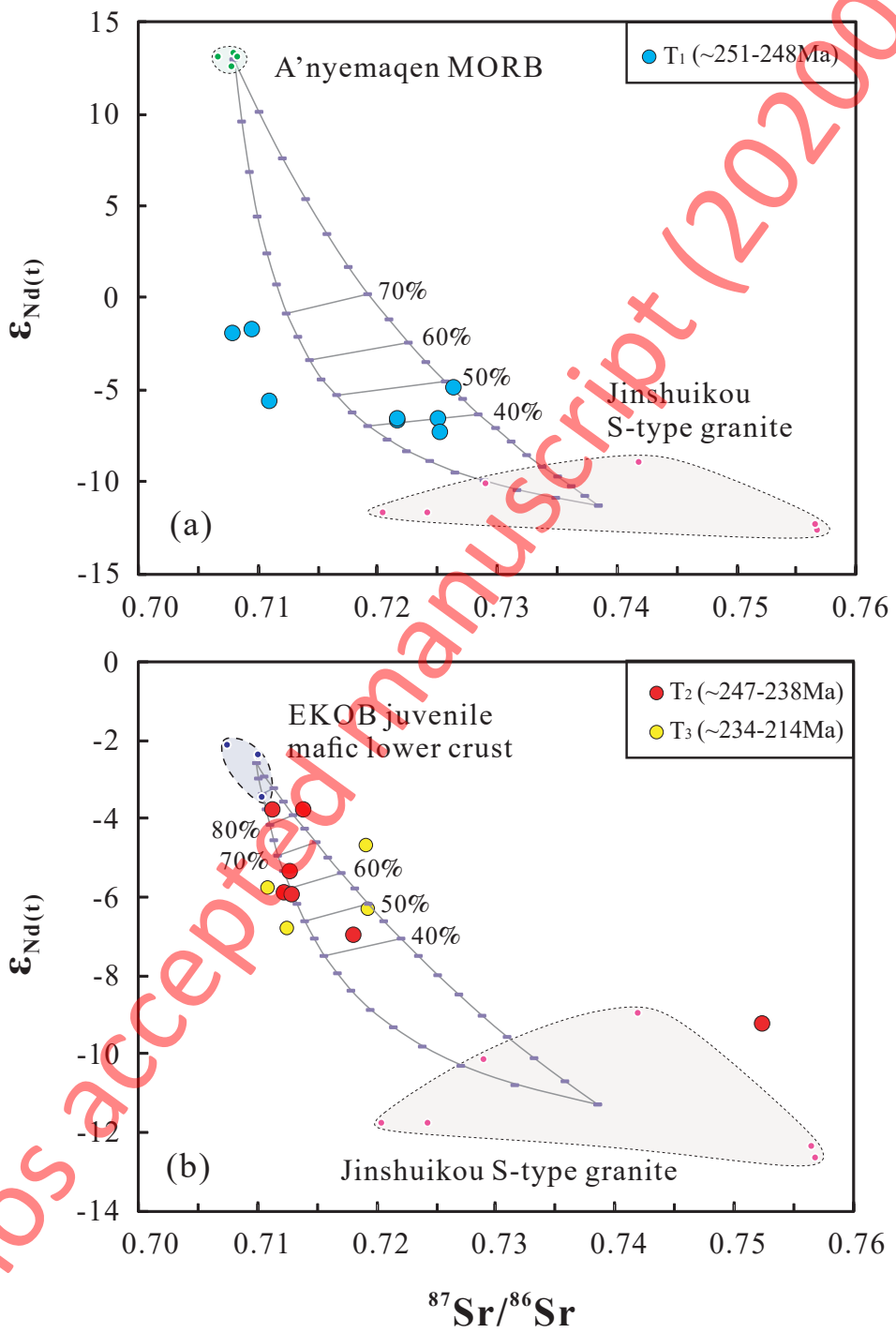
Lithos accepted manuscript (20200326)

Fig.9



Lithos accepted manuscript (20200326)

Fig. 10



Lithos accepted manuscript (20200326)

Fig. 11

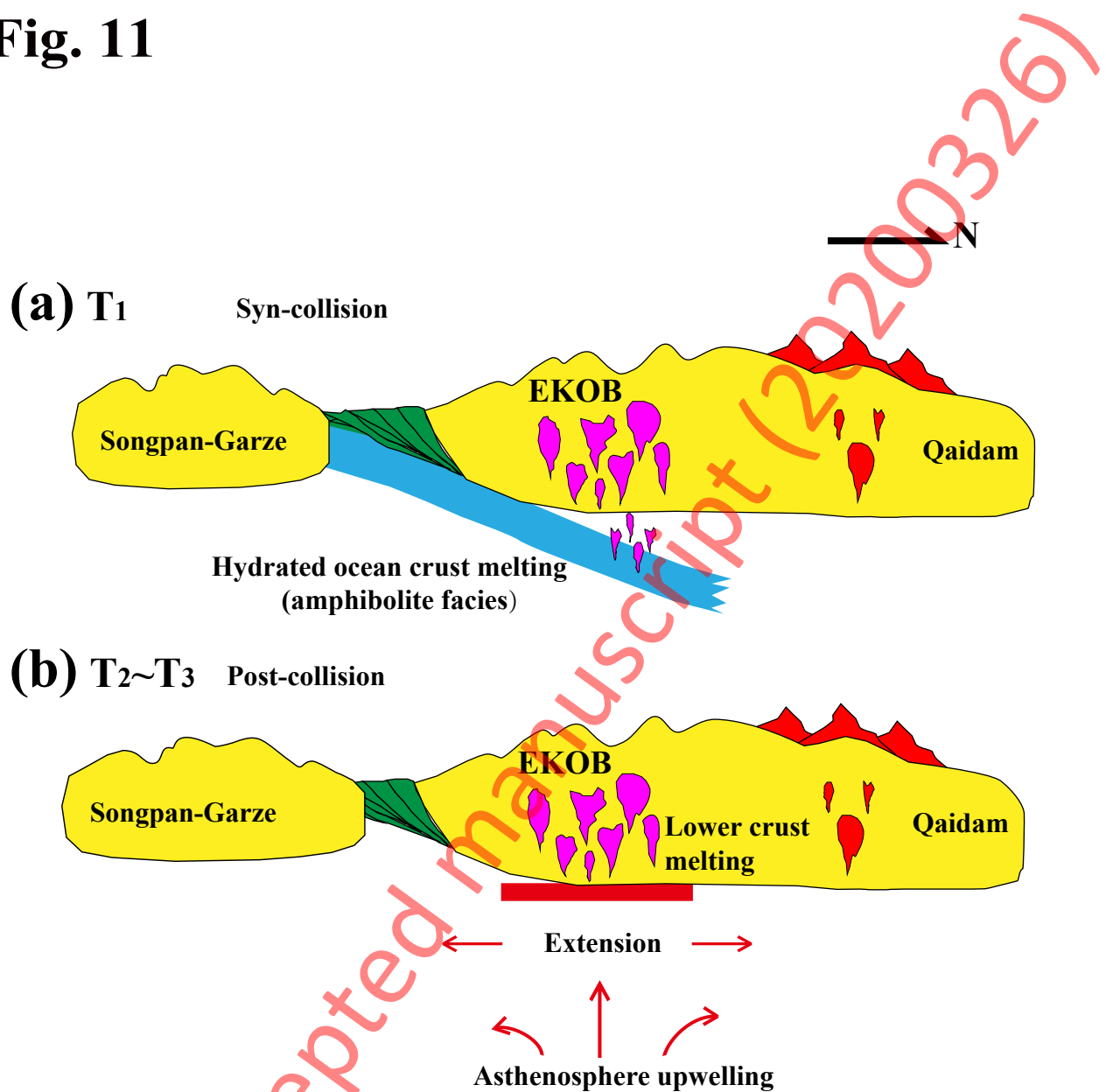


Table 1

Sample locations and zircon U-Pb ages of the Triassic granitoids in the East Kunlun Orogenic Belt.

Sample	Point	GPS	Lithology	Petrology	Age (Ma)
AKDL12-01	14	N35°50'28.3" E96°29'26.2"	syenogranite	Kfs (45%), Qtz (27%), Pl (15%), Mag (8%), Bt (5%); Kfs with kaolinization.	251.4±6.8
AKDL12-03	15	N35°50'28.2" E96°29'32.1"	moyite	Kfs (50%), Qtz (30%), Mag (7%), Amp (5%), Bt (4%), Pl (4%).	251.4±6.8
AKDL12-04	16	N35°51'27.3" E96°31'5.2"	moyite	Kfs (55%), Qtz (30%), Pl (5%), Mag (5%), Bt (5%).	251.4±6.8
BLX12-09	21	N35°48'34.9" E97°24'25.8"	granodiorite	Pl (50%), Qtz (20%), Bt (10%), Amp (5%); accessory mineral (Ap)	250.5±0.74
BLX12-03	18	N35°46'38.5" E97°22'11.2"	monzogranite	Qtz (35%), Kfs (30%), Pl (25%), Bt (10%); Kfs with kaolinization.	247.8±2.1
BLX12-06	19	N35°46'58.9" E97°22'51.1"	granite porphyry	Phenocrysts of Qtz (40%), Kfs (30%), Pl (25%), Bt (5%), Qtz and Kfs with melt corrosion shapes; groundmass with the same mineral assemblage.	247.8±2.1
BLX12-08	20	N35°47'37.2" E97°23'43.0"	monzogranite	Qtz (30%), Kfs (30%), Pl (25%), Bt+Mag (15%).	247.8±2.1
HXNC12-07	3	N36°18'53.8" E94°35'21.4"	granite	Qtz (40%), Pl (35%), Kfs (10%), Bt (10%), Mag (5%); accessory minerals (Ap+Zrn); Pl with sericitization.	247.6±4.8
NSK12-09	4	N36°8'14.6" E94°47'57.7"	syenogranite	Kfs (45%), Qtz (28%), Pl (15%), Bt (8%), Mag (4%); Kfs with kaolinization.	247.6±4.8
GYK12-05	7	N36°16'19.3" E95°23'56.6"	biotite granite	Qtz (35%), Pl (30%), Kfs (15%), Bt (20%).	246.6±1.9 ⁶
DGLX12-01	8	N36°21'23.1" E95°29'25"	granodiorite	Pl (35%), Qtz (25%), Kfs (10%), Bt+Amp+Mag (30%).	246.6±1.9 ⁶
DGL12-01	9	N36°11'33.5" E95°47'39.2"	biotite granite	Qtz (30%), Pl+Kfs (45%), Bt (20%), Mag (5%).	246.6±1.9 ⁶
DGL12-02	9	N36°11'33.5" E95°47'39.2"	biotite moyite	Kfs (45%), Qtz (30%), Bt (25%); porphyroid texture.	246.6±1.9 ⁶
HYC12-01	5	N36°12'55" E95°05'36"	biotite monzogranite	Qtz (30%), Kfs (30%), Pl (30%), Bt (10%).	245.5±9.2
HYC12-06 (host)	6	N36°14'6.3" E95°05'6.8"	biotite granite	Qtz (28%), Pl (35%), Kfs (15%), Bt (20%), Amp (2%).	245.5±9.2
WLG12-05	12	N36°15'40.5" E95°55'12.2"	syenogranite	Kfs (50%), Qtz (30%), Pl (10%), Chl (10%).	244±2 ¹
WLG12-07	13	N36°18'17" E95°54'11.4"	syenogranite	Kfs (40%), Qtz (30%), Pl (15%), Bt (15%); accessory mineral (Zrn)	244±2 ¹
HXNC12-01	1	N36°21'31.4" E94°24'37.6"	syenogranite	Kfs (48%), Qtz (32%), Pl (10%), Bt (10%).	237.8±3.8
HXNC12-05	2	N36°21'39.8" E94°24'37.8"	quartz diorite	Pl (40%), Qtz (20%), Bt+Amp (40%).	237.8±3.8
ZJX12-01	17	N36°10'27.8" E97°01'10.6"	quartz diorite	Pl (40%), Qtz (10%), Kfs (10%), Bt+Amp (35%), Mag (5%).	234.2±2.1 ⁶
BLXD12-06	24	N36°01'8.7" E97°46'17"	amphibole quartz monzonite	Kfs (30%), Pl (30%), Qtz (15%), Bt+Amp (25%).	227.1±0.74
WLS12-01	25	N36°01'33.5" E97°48'7.3"	syenogranite	Kfs (50%), Qtz (30%), Pl (12%), Bt (5%), Mag (3%).	227.1±0.74
BLX12-15 (host)	22	N35°58'39.6" E97°28'32.1"	granodiorite	Pl (45%), Qtz (25%), Kfs (5%), Bt+Amp (20%); Mag (5%).	222.02±0.91 ⁴
DGL12-05	10	N36°14'4.3" E95°46'35.7"	syenogranite	Kfs (57%), Qtz (30%), Pl (8%), Bt (5%).	215±3 ¹
DGL12-07	11	N36°14'28" E95°44'47.6"	moyite	Kfs (56%), Qtz (28%), Bt (8%), Pl (5%), Mag (3%).	215±3 ¹
BLXD12-02	23	N36°01'34.3" E97°39'4.1"	granite porphyry	Phenocrysts of Qtz and feldspar, Qtz and feldspar with melt corrosion shapes; groundmass of Kfs (50%), Qtz (30%), Bt (10%), Pl (5%), Mag (5%).	214±1 ⁷

Kfs = potash feldspar; Qtz = quartz; Pl = plagioclase; Bt = biotite; Amp = amphibole; Mag = magnetite; Ap = apatite; Zrn = zircon.

Ages with superscript are from literature being the same as that in Fig. 1.

Table 2

Whole-rock major and trace element data of the Triassic granitoids in the East Kunlun Orogenic Belt.

Sample	AKDL12-01	AKDL12-03	AKDL12-04	BLX12-09	BLX12-03	BLX12-06	BLX12-08	HXNC12-07	NSK12-09
Age (Ma)	(Early Triassic) ~ 251			~ 248					
<i>Major elements (wt.%)</i>									
SiO ₂	72.50	72.24	75.83	63.01	73.19	72.55	72.13	75.40	72.74
TiO ₂	0.44	0.41	0.10	0.65	0.13	0.13	0.13	0.11	0.14
Al ₂ O ₃	13.60	14.17	13.18	16.27	13.96	14.20	14.45	13.84	13.85
Fe ₂ O ₃ ^T	2.87	2.89	0.67	5.67	2.16	1.98	2.09	1.06	2.01
MnO	0.06	0.09	0.02	0.11	0.07	0.04	0.07	0.02	0.06
MgO	0.78	1.09	0.07	1.99	0.22	0.23	0.25	0.16	0.24
CaO	2.73	3.08	0.81	4.90	1.31	1.63	1.40	1.14	1.65
Na ₂ O	3.74	4.97	4.00	3.23	4.12	3.93	4.20	3.30	3.58
K ₂ O	2.37	0.47	4.26	3.05	3.60	3.69	3.86	4.47	4.28
P ₂ O ₅	0.09	0.08		0.17	0.04	0.06		0.03	0.04
LOI	0.71	0.99	0.44	0.49	0.52	0.67	0.53	0.52	0.54
Total	99.89	100.49	99.38	99.52	99.32	99.12	99.12	100.04	99.11
A/NK	17.09	14.07	76.26	7.33	40.97	33.73	37.25	50.11	33.42
A/CNK	0.99	0.99	1.04	0.93	1.07	1.06	1.06	1.12	1.02
Mg [#]	0.37	0.45	0.19	0.44	0.18	0.21	0.21	0.25	0.21
<i>Trace elements (ppm)</i>									
Li	4.47	9.60	2.64	21.8	40.6	14.8	39.9	33.9	50.0
Sc	7.90	7.34	1.95	13.8	3.46	2.88	3.40	3.59	2.28
V	54.6	44.4	2.07	119	4.49	4.66	4.96	3.67	4.88
Cr	4.44	3.78	17.2	10.0	4.82	21.6	4.75	3.00	3.85
Co	5.81	3.39	0.29	11.5	0.93	0.94	0.99	0.53	1.14
Ni	2.51	2.49	8.88	11.8	0.97	8.42	1.63	1.27	0.50
Cu	2.51	0.75	0.24	3.68		2.37		0.08	1.56
Zn	33.5	28.6	6.97	59.1	33.4	21.7	27.6	19.1	27.6
Ga	16.2	15.5	13.9	17.8	17.3	15.8	16.6	21.3	14.6
Rb	65.5	7.73	231	102	157	150	139	200	156
Sr	249	389	48.5	455	113	152	128	198	101
Y	19.0	21.1	15.0	22.5	29.8	21.1	25.7	19.6	18.3
Zr	206	187	56.3	189	119	101	131	96.5	105
Nb	6.94	7.95	14.2	9.77	11.9	9.81	11.4	16.3	10.0
Cs	0.52	0.86	2.60	2.22	3.31	2.72	3.06	4.41	3.42
Ba	734	268	168	845	974	995	1131	1098	447
La	28.0	25.6	22.2	31.8	35.7	37.5	35.6	40.7	19.2
Ce	55.2	51.5	42.2	64.7	68.8	69.7	67.8	80.5	35.4
Pr	5.89	5.57	4.20	7.29	7.34	7.17	7.16	8.85	3.63
Nd	21.3	20.2	13.6	28.0	25.8	24.6	25.0	32.7	12.4
Sm	3.81	3.81	2.53	5.35	4.96	4.34	4.61	6.43	2.55
Eu	1.07	0.85	0.26	1.37	0.73	0.76	0.82	0.96	0.53
Gd	3.53	3.60	2.28	4.85	4.73	3.91	4.36	5.45	2.59
Tb	0.51	0.54	0.34	0.68	0.76	0.57	0.67	0.72	0.43
Dy	3.13	3.43	2.08	4.01	4.76	3.49	4.16	3.81	2.75
Ho	0.66	0.74	0.45	0.81	1.00	0.71	0.87	0.65	0.58
Er	2.12	2.32	1.48	2.45	3.12	2.18	2.69	1.71	1.80
Tm	0.31	0.35	0.23	0.34	0.46	0.32	0.40	0.22	0.28
Yb	2.18	2.40	1.72	2.25	3.18	2.21	2.70	1.30	1.97
Lu	0.34	0.37	0.28	0.33	0.48	0.33	0.41	0.17	0.30
Hf	4.82	4.48	1.88	4.33	3.43	2.79	3.54	3.26	2.96
Ta	0.52	0.52	0.85	0.67	0.75	0.79	0.74	1.11	0.86
Pb	9.12	7.08	15.7	13.6	20.9	14.5	19.1	36.5	22.9
Th	7.45	8.34	25.4	10.0	14.7	16.3	13.9	8.36	13.2
U	1.26	1.38	1.29	1.34	1.72	1.35	1.59	1.59	2.22
(La/Yb) _N	9.22	7.65	9.25	10.13	8.05	12.20	9.46	22.44	6.98
Eu/Eu [*]	0.89	0.70	0.33	0.82	0.46	0.57	0.56	0.50	0.63
Sr/Sr [*]	0.65	1.06	0.19	0.92	0.24	0.33	0.28	0.34	0.44

(continued)

Table 2 (continued)

Sample	GYK12-05	DGLX12-01	DGL12-01	DGL12-02	HYC12-01	HYC12-06 (host)	WLG12-05	WLG12-07	HXNC12-01
Age (Ma)	(Middle Triassic)	~ 247			~ 246		~ 244		~ 238
<i>Major elements (wt.%)</i>									
SiO ₂	70.68	69.16	67.32	69.08	71.35	68.42	71.12	72.95	68.01
TiO ₂	0.31	0.37	0.57	0.61	0.19	0.39	0.25	0.22	0.43
Al ₂ O ₃	14.83	14.63	16.33	13.83	14.96	15.93	14.20	13.19	15.87
Fe ₂ O ₃ ^T	2.79	3.35	3.60	4.11	1.95	3.13	2.37	1.76	3.02
MnO	0.06	0.07	0.05	0.06	0.06	0.06	0.09	0.02	0.06
MgO	0.62	1.41	1.70	1.19	0.44	1.04	0.58	0.28	0.87
CaO	2.72	3.67	4.11	2.50	2.52	4.21	1.77	0.96	3.27
Na ₂ O	3.55	3.24	3.29	2.66	4.21	4.05	3.28	3.55	3.76
K ₂ O	3.16	2.72	1.43	4.23	2.72	1.18	4.37	4.94	3.40
P ₂ O ₅	0.05	0.07	0.12	0.15	0.07	0.13	0.05	0.02	0.15
LOI	0.49	0.61	0.88	1.12	0.51	0.51	1.54	1.48	0.48
Total	99.25	99.30	99.40	99.53	98.97	99.06	99.64	99.37	99.33
A/NK	17.83	10.97	9.28	14.82	20.59	10.91	24.67	48.54	13.68
A/CNK	1.04	0.98	1.13	1.02	1.03	1.02	1.06	1.02	1.00
Mg [#]	0.33	0.48	0.51	0.39	0.33	0.42	0.35	0.26	0.39
<i>Trace elements (ppm)</i>									
Li	65.0	41.2	52.2	57.9	38.4	16.9	15.0	18.7	33.2
Sc	3.70	5.97	10.0	9.92	2.09	2.89	4.92	3.00	3.67
V	10.5	46.8	60.8	35.4	10.9	22.0	20.8	7.99	27.9
Cr	2.75	10.1	31.1	11.1	4.06	5.31	5.74	5.15	3.97
Co	2.04	6.36	5.90	6.43	1.57	3.28	2.03	1.13	3.39
Ni	0.70	5.07	8.68	2.78	0.90	2.17	2.72	1.45	1.62
Cu	0.37	1.33	1.38	4.75		0.16	3.61	0.44	0.54
Zn	58.1	50.5	50.0	80.5	53.2	56.8	50.3	43.5	48.4
Ga	19.6	16.5	20.3	21.9	20.0	16.9	16.8	20.6	19.0
Rb	117	105	102	260	76.0	38.4	149	257	131
Sr	297	397	311	134	406	569	257	57.1	458
Y	13.5	10.8	13.3	24.4	6.27	3.91	12.0	43.7	8.60
Zr	153	107	184	281	92.1	111	167	227	197
Nb	13.1	7.56	7.13	13.0	10.4	5.45	12.9	14.4	9.50
Cs	3.96	3.18	10.3	10.1	2.55	0.72	2.99	5.04	1.91
Ba	471	697	240	546	852	420	1298	282	818
La	20.0	21.4	20.6	47.9	27.6	22.1	40.6	46.2	28.5
Ce	39.2	39.4	43.6	104	51.4	41.8	70.8	102	51.7
Pr	4.34	4.19	5.00	11.6	5.16	4.47	6.89	11.1	5.49
Nd	15.7	15.0	19.4	43.2	17.1	15.5	23.0	41.5	19.4
Sm	3.15	2.70	3.83	7.76	2.47	2.14	3.84	8.64	3.20
Eu	0.65	0.81	1.03	1.09	0.78	0.86	0.84	0.40	0.86
Gd	2.84	2.39	3.43	6.28	1.83	1.50	3.25	8.15	2.46
Tb	0.43	0.32	0.47	0.81	0.22	0.16	0.42	1.22	0.30
Dy	2.46	1.86	2.59	4.37	1.10	0.74	2.25	7.39	1.55
Ho	0.47	0.38	0.50	0.85	0.20	0.13	0.43	1.52	0.29
Er	1.32	1.12	1.41	2.49	0.57	0.37	1.20	4.57	0.83
Tm	0.19	0.16	0.20	0.35	0.08	0.05	0.16	0.65	0.11
Yb	1.23	1.09	1.28	2.29	0.51	0.32	1.02	4.27	0.79
Lu	0.17	0.17	0.19	0.35	0.08	0.05	0.16	0.62	0.12
Hf	3.86	2.70	4.24	6.40	2.70	2.74	4.01	6.32	4.59
Ta	0.80	0.50	0.44	0.88	0.70	0.38	0.79	0.92	0.64
Pb	19.2	14.6	13.3	26.9	16.2	7.41	28.2	22.8	18.6
Th	6.64	9.42	5.71	24.3	4.89	3.83	17.7	21.9	8.04
U	1.04	1.75	1.25	3.96	0.69	0.43	1.45	4.33	0.99
(La/Yb) _N	11.67	14.14	11.49	15.00	38.72	49.23	28.46	7.77	25.83
Eu/Eu [*]	0.67	0.98	0.87	0.48	1.12	1.47	0.73	0.15	0.94
Sr/Sr [*]	1.04	1.45	0.91	0.17	1.25	1.98	0.59	0.08	1.28

(continued)

Table 2 (continued)

Sample	HXNC12-05	ZJX12-01 (Late Triassic)	WLS12-01	BLX12-15 (host)	DGL12-05	DGL12-07	BLXD12-02
Age (Ma)	~ 238	~ 234	~ 227	~ 222	~ 215	~ 214	
<i>Major elements (wt.%)</i>							
SiO ₂	60.06	63.86	74.78	64.10	74.75	73.38	72.82
TiO ₂	0.95	0.68	0.10	0.66	0.17	0.21	0.24
Al ₂ O ₃	16.06	16.81	12.94	15.72	12.72	13.32	13.29
Fe ₂ O ₃ ^T	7.29	4.33	1.47	4.50	1.60	1.90	2.44
MnO	0.10	0.07	0.04	0.07	0.01	0.03	0.04
MgO	2.96	1.88	0.12	2.05	0.21	0.15	0.48
CaO	6.02	4.40	0.94	4.27	0.76	0.85	1.66
Na ₂ O	3.26	3.65	3.58	3.59	3.34	3.62	3.54
K ₂ O	1.94	3.16	4.47	2.59	5.02	5.55	3.65
P ₂ O ₅	0.24	0.17	0.03	0.18	0.02	0.05	0.14
LOI	1.60	0.84	0.76	1.27	0.70	0.56	1.08
Total	100.48	99.86	99.24	99.01	99.31	99.61	99.39
A/NK	5.27	8.11	61.55	8.00	63.95	62.73	28.13
A/CNK	0.87	0.96	1.04	0.95	1.03	0.98	1.04
Mg [#]	0.47	0.49	0.15	0.50	0.22	0.15	0.30
<i>Trace elements (ppm)</i>							
Li	49.0	48.4	10.7	15.9	15.9	21.3	24.5
Sc	18.3	8.15	2.11	10.3	2.18	2.83	3.83
V	153	60.4	2.19	100	3.15	6.55	19.5
Cr	17.9	14.7	18.4	17.5	2.65	10.3	8.11
Co	15.4	7.04	0.64	10.9	0.55	0.89	2.59
Ni	5.91	5.05	8.16	6.52	0.48	5.47	4.69
Cu	6.08	1.61	2.03	1.66	0.59	0.17	2.37
Zn	68.1	58.9	23.3	49.6	42.1	45.6	44.6
Ga	20.8	19.7	17.4	20.3	20.7	22.5	16.9
Rb	87.7	132	158	94.1	244	205	157
Sr	387	422	153	497	28.4	39.9	153
Y	18.8	15.4	10.8	14.4	49.5	33.1	31.4
Zr	136	196	102	159	208	272	136
Nb	11.3	10.2	11.7	11.9	13.4	12.4	28.5
Cs	2.40	10.8	2.51	3.71	7.24	6.04	4.66
Ba	357	534	2012	684	173	235	507
La	37.9	24.2	48.3	31.9	61.6	89.7	29.4
Ce	72.9	49.4	89.8	63.5	129	186	63.8
Pr	8.04	5.73	8.85	6.83	14.0	19.1	7.39
Nd	31.4	21.4	29.2	24.5	50.1	68.0	27.3
Sm	5.88	4.16	4.24	4.28	10.1	11.4	5.76
Eu	1.22	1.06	0.94	1.09	0.30	0.41	0.65
Gd	5.37	3.54	3.18	3.63	9.29	9.38	5.28
Tb	0.71	0.48	0.38	0.48	1.40	1.21	0.82
Dy	3.89	2.68	1.94	2.63	8.53	6.64	5.12
Ho	0.74	0.51	0.36	0.50	1.69	1.28	1.06
Er	2.02	1.44	1.08	1.43	4.89	3.67	3.28
Tm	0.25	0.19	0.15	0.20	0.66	0.48	0.49
Yb	1.52	1.30	1.03	1.29	4.36	3.07	3.31
Lu	0.22	0.18	0.16	0.19	0.61	0.44	0.48
Hf	3.23	4.68	2.48	3.90	6.38	6.96	3.73
Ta	0.81	0.60	0.69	0.78	0.84	0.88	1.86
Pb	10.8	18.7	23.3	10.7	26.4	25.2	20.9
Th	5.23	8.00	14.7	11.2	22.5	17.4	22.5
U	0.80	1.46	2.23	1.79	2.97	1.96	2.61
(La/Yb) _N	17.84	13.41	33.59	17.77	10.12	20.94	6.37
Eu/Eu*	0.67	0.84	0.78	0.85	0.09	0.12	0.36
Sr/Sr*	0.71	1.11	0.28	1.11	0.03	0.03	0.31

A/NK = molar Al₂O₃/(Na₂O+K₂O), A/CNK = molar Al₂O₃/(CaO+Na₂O+K₂O), Mg[#] = molar Mg/(Mg+Fe²⁺); LOI, loss on ignition.(La/Yb)_N refers to the value normalized against chondrite. Eu/Eu* = Eu_{PM}/[Sm_{PM}×Gd_{PM}]^{1/2}, Sr/Sr* = Sr_{PM}/[Pr_{PM}×Nd_{PM}]^{1/2}, where subscript PM denotes normalized values against primary mantle.

Table 3

Whole rock Sr-Nd-Hf isotopic composition of the Triassic granitoids from the East Kunlun Orogenic Belt.

Sample	Rb (ppm)	Sr (ppm)	$^{87}\text{Rb}/^{86}\text{Sr}$	$^{87}\text{Sr}/^{86}\text{Sr}$	$\pm 2\sigma$	I_{sr}	Sm (ppm)	Nd (ppm)	$^{147}\text{Sm}/^{144}\text{Nd}$	$^{143}\text{Nd}/^{144}\text{Nd}$	$\pm 2\sigma$	$^{143}\text{Nd}/^{144}\text{Nd}$	$\epsilon_{\text{Nd}}(t)$	Lu (ppm)	Hf (ppm)	$^{176}\text{Lu}/^{177}\text{Hf}$	$^{176}\text{Hf}/^{177}\text{Hf}$	$\pm 2\sigma$	$^{176}\text{Hf}/^{177}\text{Hf}_i$	$\epsilon_{\text{Hf}}(t)$	t (Ma)
<i>T₁ group</i>																					
BLX12-09	102	455	0.65	0.710934	6	0.708626	5.35	28.0	0.12	0.512222	3	0.512030	-5.55	0.33	4.33	0.01	0.282553	2	0.282501	-4.06	251
AKDL12-01	65.5	249	0.76	0.709400	5	0.706684	3.81	21.3	0.11	0.512409	4	0.512230	-1.66	0.34	4.82	0.01	0.282765	2	0.282718	3.59	251
AKDL12-03	7.73	389	0.06	0.707823	3	0.707617	3.81	20.2	0.11	0.512405	6	0.512216	-1.92	0.37	4.48	0.01	0.282762	2	0.282707	3.21	251
HXNC12-07	200	198	2.92	0.725152	5	0.714843	6.43	32.7	0.12	0.512138	5	0.511944	-7.32	0.17	3.26	0.01	0.282509	3	0.282474	-5.11	248
NSK12-09	156	101	4.46	0.726310	6	0.710573	2.55	12.4	0.12	0.512272	4	0.512069	-4.88	0.30	2.96	0.01	0.282636	3	0.282569	-1.74	248
BLX12-03	157	113	4.01	0.725105	5	0.710972	4.96	25.8	0.12	0.512171	3	0.511981	-6.59	0.48	3.43	0.02	0.282588	3	0.282496	-4.31	248
BLX12-06	150	152	2.87	0.721635	3	0.711511	4.34	24.6	0.11	0.512153	3	0.511979	-6.64	0.33	2.79	0.02	0.282577	3	0.282499	-4.20	248
BLX12-08	139	128	3.13	0.721689	5	0.710650	4.61	25.0	0.11	0.512167	3	0.511985	-6.52	0.41	3.54	0.02	0.282584	3	0.282508	-3.88	248
AKDL12-04	231	48.5	13.80	0.755502	5	0.706213	2.53	13.6	0.11	0.512332	4	0.512146	-3.30	0.28	1.88	0.02	0.282713	4	0.282615	-0.05	251
<i>T₂ group</i>																					
GYK12-05	117	297	1.15	0.718030	4	0.714006	3.15	15.7	0.12	0.512161	5	0.511963	-6.97	0.17	3.86	0.01	0.282512	2	0.282483	-4.81	247
DGLX12-01	105	397	0.77	0.711228	5	0.708529	2.70	15.0	0.11	0.512304	4	0.512127	-3.76	0.17	2.70	0.01	0.282633	3	0.282592	-0.93	247
DGL12-02	260	134	5.60	0.752345	4	0.732679	7.76	43.2	0.11	0.512025	3	0.511848	-9.21	0.35	6.40	0.01	0.282443	3	0.282407	-7.50	247
HYC12-06 (host)	38.4	569	0.20	0.712135	5	0.711452	2.14	15.5	0.08	0.512157	4	0.512022	-5.85	0.05	2.74	0.00	0.282532	3	0.282520	-3.51	246
WLG12-05	149	257	1.68	0.713781	3	0.707954	3.84	23.0	0.10	0.512294	3	0.512131	-3.76	0.16	4.01	0.01	0.282619	3	0.282594	-0.96	244
HXNC12-01	131	458	0.83	0.712664	5	0.709853	3.20	19.4	0.10	0.512214	3	0.512058	-5.35	0.12	4.59	0.00	0.282558	2	0.282541	-2.94	238
HXNC12-05	87.7	387	0.66	0.712885	4	0.710665	5.88	31.4	0.11	0.512205	4	0.512027	-5.94	0.22	3.23	0.01	0.282554	3	0.282511	-4.01	238
<i>T₃ group</i>																					
ZJX12-01	132	422	0.91	0.712378	4	0.709362	4.16	21.4	0.12	0.512172	4	0.511990	-6.76	0.18	4.68	0.01	0.282481	3	0.282456	-6.04	234
WLS12-01	158	153	2.99	0.718922	4	0.709265	4.24	29.2	0.09	0.512239	5	0.512108	-4.65	0.16	2.48	0.01	0.282575	3	0.282536	-3.36	227
BLX12-15 (host)	94.1	497	0.55	0.710661	5	0.708930	4.28	24.5	0.11	0.512213	3	0.512059	-5.73	0.19	3.90	0.01	0.282557	2	0.282529	-3.74	222
DGL12-05	244	28.4	24.95	0.855875	5	0.779601	10.1	50.1	0.12	0.512224	3	0.512051	-6.05	0.61	6.38	0.01	0.282655	3	0.282601	-1.34	215
DGL12-07	205	39.9	14.90	0.800046	4	0.754482	11.4	68.0	0.10	0.512180	4	0.512036	-6.34	0.44	6.96	0.01	0.282604	3	0.282567	-2.53	215
BLXD12-02	157	153	2.97	0.719073	4	0.710046	5.76	27.3	0.13	0.512221	4	0.512041	-6.27	0.48	3.73	0.02	0.282586	3	0.282512	-4.49	214

$$I_{\text{sr}} = [({}^{87}\text{Sr}/{}^{86}\text{Sr}) - ({}^{87}\text{Rb}/{}^{86}\text{Sr})(e^{\lambda t} - 1)]; {}^{143}\text{Nd}/{}^{144}\text{Nd}_i = [({}^{143}\text{Nd}/{}^{144}\text{Nd}) - ({}^{147}\text{Sm}/{}^{144}\text{Nd})(e^{\lambda t} - 1)]; \epsilon_{\text{Nd}}(t) = [({}^{143}\text{Nd}/{}^{144}\text{Nd})/({}^{143}\text{Nd}/{}^{144}\text{Nd}_{\text{CHUR}}) - 1] \times 10^4; {}^{176}\text{Hf}/{}^{177}\text{Hf}_i = [({}^{176}\text{Hf}/{}^{177}\text{Hf}) - ({}^{176}\text{Lu}/{}^{177}\text{Hf})(e^{\lambda t} - 1)]; \epsilon_{\text{Hf}}(t) = [({}^{176}\text{Hf}/{}^{177}\text{Hf})/({}^{176}\text{Hf}/{}^{177}\text{Hf}_{\text{CHUR}}) - 1] \times 10^4.$$

$${}^{147}\text{Sm}/{}^{144}\text{Nd}_{\text{CHUR}} = 0.1967; {}^{143}\text{Nd}/{}^{144}\text{Nd}_{\text{CHUR}} = 0.512638; {}^{176}\text{Lu}/{}^{177}\text{Hf}_{\text{CHUR}} = 0.0332; {}^{176}\text{Hf}/{}^{177}\text{Hf}_{\text{CHUR}} = 0.282772; \lambda({}^{87}\text{Rb}) = 1.42 \times 10^{-11} \text{ yr}^{-1}; \lambda({}^{147}\text{Sm}) = 6.54 \times 10^{-12} \text{ yr}^{-1}, \lambda({}^{176}\text{Lu}) = 1.865 \times 10^{-11} \text{ yr}^{-1}.$$